KEPLER ECLIPSING BINARY STARS. VII. the CATALOG of ECLIPSING BINARIES FOUND in the ENTIRE KEPLER DATA SET

Brian Kirk
National Radio Astronomy Observatory

Kyle Conroy
Villanova University

Andrej Prša
Vanderbilt University

Michael Abdul-Masih
Vanderbilt University

Angela Kochoska
Univerza v Ljubljani

See next page for additional authors

Follow this and additional works at: https://digitalcommons.lsu.edu/physics_astronomy_pubs

Recommended Citation

Authors

Brian Kirk, Kyle Conroy, Andrej Prša, Michael Abdul-Masih, Angela Kochoska, Gal Matijevič, Kelly Hambleton, Thomas Barclay, Steven Bloemen, Tabetha Boyajian, Laurance R. Doyle, B. J. Fulton, Abe Johannes Hoekstra, Kian Jek, Stephen R. Kane, Veselin Kostov, David Latham, Tsevi Mazeh, Jerome A. Orosz, Joshua Pepper, Billy Quarles, Darin Ragozzine, Avi Shporer, John Southworth, Keivan Stassun, Susan E. Thompson, William F. Welsh, Eric Agol, Aliz Derekas, Jonathan Devor, Debra Fischer, Gregory Green, and Jeff Gropp

KEPLER ECLIPSING BINARY STARS. VII. the CATALOG of ECLIPSING BINARIES FOUND in the ENTIRE KEPLER DATA SET

Document Version
Final published version

[Link to publication record in Manchester Research Explorer](#)

Citing this paper
Please note that where the full-text provided on Manchester Research Explorer is the Author Accepted Manuscript or Proof version this may differ from the final Published version. If citing, it is advised that you check and use the publisher's definitive version.

KEPLER ECLIPSING BINARY STARS. VII. THE CATALOG OF ECLIPSING BINARIES FOUND IN THE ENTIRE KEPLER DATA SET

Brian Kirk[1,2], Kyle Conroy[2,3], Andrej Prša[3], Michael Abdul-Masih[3,4], Angela Kochoska[5], Gal Matijevič[3], Kelly Hambleton[6], Thomas Barclay[7], Steven Bloemen[8], Tabetha Boyajian[9], Laurance R. Doyle[10,11], B. J. Fulton[12], Abe Johannes Hoekstra[35], Kian Jek[35], Stephen R. Kane[13], Veselin Kostov[14], David Latham[15], Tsevi Mazeh[16], Jerome A. Orosz[17], Joshua Pepper[18], Billy Quarles[19], Darin Ragozzine[20], Avi Shporer[21,36], John Southworth[22], Keivan Stassun[23], Susan E. Thompson[24], William F. Welsh[17], Eric Agol[25], Aliz Derekas[26,27], Jonathan Devor[28], Debra Fischer[29], Gregory Green[30], Jeff Gropp[2], Tom Jacobs[35], Cole Johnston[2], Daryll Matthew LaCourse[35], Kristian Saetre[35], Hans Schwengeler[31], Jacek Toczyski[32], Griffin Werner[2], Matthew Garrett[17], Joanna Gore[17], Arturo O. Martinez[17], Isaac Spitzer[17], Justin Stevick[17], Pantelis C. Thomadis[17], Eliot Halley Vrijmoet[17], Mitchell Yenawine[17], Natalie Batalha[33], and William Borucki[34]

[1] National Radio Astronomy Observatory, North American ALMA Science Center, 520 Edgemont Road, Charlottesville, VA 22903, USA; bkirk@nrao.edu
[2] Villanova University, Dept. of Astrophysics and Planetary Science, 800 E Lancaster Ave, Villanova, PA 19085, USA; aprsa@villanova.edu
[3] Vanderbilt University, Dept. of Physics and Astronomy, VU Station B 1807, Nashville, TN 37235, USA; kyle.conroy@vanderbilt.edu
[4] Rensselaer Polytechnic Institute, Dept. of Physics, Applied Physics, and Astronomy, 110 8th St, Troy, NY 12180, USA
[5] Faculty of Mathematics and Physics, University of Ljubljana, Jadranska 19, 1000 Ljubljana, Slovenia
[6] Jeremiah Horrocks Institute, University of Central Lancashire, Preston, PR1 2HE, England
[7] NASA Ames Research Center/BAER Institute, Moffett Field, CA 94035, USA
[8] Department of Astrophysics/IMAPP, Radboud University Nijmegen, 6500 GL Nijmegen, The Netherlands
[9] J.W. Gibbs Laboratory, Yale University, 260 Whitney Avenue, New Haven, CT 06511, USA
[10] IMoP at Principia College, Elsah, IL 62028, USA
[11] SETI Institute, 189 Bernardo Ave. Mountain View, CA 94043, USA
[12] Las Cumbres Observatory Global Telescope Network, Goleta, CA 93117, USA
[13] San Francisco State University, 1600 Holloway Avenue, San Francisco, CA 94132, USA
[14] Department of Astronomy & Astrophysics at U of T, Toronto, Ontario, M5S 3H4, Canada
[15] Harvard-Smithsonian Center for Astrophysics, 60 Garden Street, Cambridge, MA 02138, USA
[16] Wise Observatory, Tel Aviv University, Tel Aviv, Israel
[17] San Diego State University, 5500 Campanile Dr., San Diego, CA 92182, USA
[18] Lehigh University, Department of Physics, 16 Memorial Drive East, Bethlehem, PA 18015, USA
[19] NASA Ames Research Center, Astrobiology and Space Science Division MS 245-3, Moffett Field, CA 94035, USA
[20] Florida Institute of Technology, Physics and Space Sciences, 150 W. University Blvd. Melbourne, FL 32901, USA
[21] Jet Propulsion Laboratory, California Institute of Technology, 4800 Oak Grove Drive, Pasadena, CA 91109, USA
[22] Astrophysics Group, Keele University, Staffordshire, ST5 5BG, UK
[23] Vanderbilt University, Nashville, TN 37240, USA
[24] SETI Institute/NASA Ames Research Center, Moffett Field, CA 94035, USA
[25] Astronomy Department, University of Washington, Seattle, WA 98195, USA
[26] ELTE Gothard Astrophysical Observatory, H-9704 Szombathely, Szent Imre herceg u. 112, Hungary
[27] Konkoly Observatory, Research Centre for Astronomy and Earth Sciences, Hungarian Academy of Sciences, H-1121, Hungary
[28] Tel Aviv University, Department of Astrophysics, Tel Aviv 69978, Israel
[29] Yale University, New Haven, CT 06520-8101, USA
[30] Harvard-Smithsonian Center for Astrophysics, 60 Garden Street, MS-10, Cambridge, MA 02138, USA
[31] Astronomisches Institut der Universitat Basel, Venusstrasse 7, CH-4102 Binningen, Switzerland
[32] University of Virginia, 4040 Lewis and Clark Dr., Charlottesville, VA 22911, USA
[33] San Jose State University, One Washington Square, San Jose, CA 95192, USA
[34] NASA Ames Research Center, Moffett Field, CA 94035, USA

ABSTRACT

The primary Kepler Mission provided nearly continuous monitoring of ~200,000 objects with unprecedented photometric precision. We present the final catalog of eclipsing binary systems within the 105 deg^2 Kepler field of view. This release incorporates the full extent of the data from the primary mission (Q0-Q17 Data Release). As a result, new systems have been added, additional false positives have been removed, ephemerides and principal parameters have been recomputed, classifications have been revised to rely on analytical models, and eclipse timing variations have been computed for each system. We identify several classes of systems including those that exhibit tertiary eclipse events, systems that show clear evidence of additional bodies, heartbeat systems, systems with changing eclipse depths, and systems exhibiting only one eclipse event over the duration of the mission. We have updated the period and galactic latitude distribution diagrams and included a catalog completeness evaluation. The total number of identified eclipsing and ellipsoidal binary systems in the Kepler field of view has increased to 2878, 1.3% of all observed Kepler targets. An online version of this catalog with downloadable content and visualization tools is maintained at http://keplerEBs.villanova.edu.

Key words: binaries: eclipsing – catalogs – methods: data analysis – methods: numerical – stars: fundamental parameters – stars: statistics

---

[35] Planet Hunter; planethunters.org.
[36] Sagan Fellow.

1. INTRODUCTION

The contribution of binary stars and, in particular, eclipsing binaries (EBs) to astrophysics cannot be overstated. EBs can provide fundamental mass and radius measurements for the component stars (e.g., see the extensive review by Andersen 1991). These mass and radius measurements in turn allow for accurate tests of stellar evolution models (e.g., Pols et al. 1997; Schroder et al. 1997; Guinan et al. 2000; Torres & Ribas 2002). In cases where high-quality radial velocity (RV) measurements exist for both stars in an EB, the luminosities computed from the absolute radii and effective temperatures can lead to a distance determination. Indeed, EBs are becoming widely used to determine distances to the Magellanic Clouds, M31, and M33 (Guinan et al. 1998; Wyithe & Wilson 2001, 2002; Ribas et al. 2002; Bonanos et al. 2003, 2006; Hilditch et al. 2005; North et al. 2010).

Large samples are useful to determine statistical properties and for finding rare binaries which may hold physical significance (for example, binaries with very low mass stars, binaries with stars in short-lived stages of evolution, very eccentric binaries that show large apsidal motion, etc.). Catalogs of EBs from ground-based surveys suffer from various observational biases such as limited accuracy per individual measurement, complex window functions (e.g., observations from ground based surveys can only be done during nights with clear skies and during certain seasons).

The NASA *Kepler* Mission, launched in 2009 March, provided essentially uninterrupted, ultra-high precision photometric coverage of ~200,000 objects within a 105 deg^2 field of view in the constellations of Cygnus and Lyra for four consecutive years. The details and characteristics of the *Kepler* instrument and observing program can be found in Batalha et al. (2010), Borucki et al. (2011), Caldwell et al. (2010), Koch et al. (2010). The mission has revolutionized the exoplanetary and EB field. The previous catalogs can be found in Prša et al. (2011, hereafter Paper I) and Slawson et al. (2011, hereafter Paper II) at http://keplerEBs.villanova.edu/v1 and http://keplerEBs.villanova.edu/v2, respectively. The current catalog and information about its functionality is available at http://keplerEBs.villanova.edu.

2. THE CATALOG

The *Kepler* Eclipsing Binary Catalog lists the stellar parameters from the Kepler Input Catalog (KIC) augmented by: primary and secondary eclipse depth, eclipse width, separation of eclipse, ephemeris, morphological classification parameter, and principal parameters determined by geometric analysis of the phased light curve.

The online Catalog also provides the raw and detrended data for ~30 minutes (long) cadence, and raw ~1 minutes (short) cadence data (when available), an analytic approximation via a polynomial chain (polyfit; Prša et al. 2008), and eclipse timing variations (ETV; Conroy et al. 2014, hereafter Paper IV and J. Orosz et al. 2016, in preparation). The construction of the Catalog consists of the following steps (1) EB signature detection (Section 3); (2) data detrending: all intrinsic variability (such as chromospheric activity, etc.) and extrinsic variability (i.e., third light contamination and instrumental artifacts) are removed by the iterative fitting of the photometric baseline (Prša et al. 2011); (3) the determination of the ephemeris: the time-space data are phase-folded and the

dispersion minimized; (4) Determination of ETVs (Section 8.6); (5) analytic approximation: every light curve is fit by a polyfit (Prša et al. 2008); (6) morphological classification via Locally Linear Embedding (LLE; Section 6), a nonlinear dimensionality reduction tool is used to estimate the "detachedness" of the system (Matijevič et al. 2012, hereafter Paper III); (7) EB characterization through geometric analysis and (8) diagnostic plot generation for false positive (FP) determination. Additional details on these steps can be found in Papers I, II, III, and IV. For inclusion in this Catalog we accept bonafide EBs and systems that clearly exhibit binarity through photometric analysis (heartbeats and ellipsoidals (Section 8.1). Throughout the Catalog and online database we use a system of subjective flagging to label and identify characteristics of a given system that would otherwise be difficult to validate quantitatively or statistically. Examples of these flags and their uses can be seen in Section 8. Although best efforts have been taken to provide accurate results, we caution that not all systems marked in the Catalog are guaranteed to be EB systems. There remains the possibility that some grazing EB signals may belong to small planet candidates or are contaminated by non-target EB signals. An in-depth discussion on Catalog completeness is presented in Section 10.

In this release, we have updated the Catalog in the following ways:

1. The light curves of *Kepler* Objects of Interest (KOIs) once withheld as possibly containing planetary transit events but since rejected have been included.
2. An increased baseline allowed for ETVs to be determined and therefore a greater precision of all ephemerides (Orosz 2012; Conroy et al. 2014). Systems previously having indeterminable periods were re-examined and included, if additional eclipses were observed.
3. Period and BJD$_0$ error estimates are provided across the Catalog. The period error analysis is derived from error propagation theory and applied through an adaptation of the Period Error Calculator algorithm of Mighell & Plavchan (2013) and BJD$_0$ errors are estimated by fitting a Gaussian to the bisected primary eclipse.
4. Quarter Amplitude Mismatch (QAM) systems have been rectified by scaling the affected season(s) to the season with the largest amplitude; a season being one of the four rotations per year to align the solar arrays. Once corrected, the system was reprocessed by the standard pipeline.
5. An additional 13 systems identified by the independent Eclipsing Binary Factory (EBF) pipeline (Section 3.2) have been processed and added to the Catalog.
6. Additional systems identified by Planet Hunters (Section 3.3), a citizen science project that makes use of the Zooniverse toolset to serve flux-corrected light curves from the public *Kepler* data set, have been added.
7. All systems were investigated to see if the signal was coming from the target source or a nearby contaminating signal. If a target was contaminated, the contaminated target was removed and the real source, if a *Kepler* target, was added to the Catalog (Section 4). A follow-up paper (M. Abdul-Masih et al. 2016, in preparation) will address the EBs that are not *Kepler* targets, but whose light curves can be recovered from target pixel files (TPFs) to a high precision and fidelity.

8. Long-cadence exposure causes smoothing of the light curves due to ∼30-minutes integration times (Section 5). Deconvolution of the phased long-cadence data polyfit allowed removal of integration smoothing, resulting in a better representation of the actual EB signal.
9. Classifications were done via LLE (Section 6), a general nonlinear dimensionality reduction tool, to give a value between 0 and 1, to represent detachedness as in Matijevič et al. (2012).
10. Visualization of the data set through tSNE (Maaten & Hinton 2008) has been provided to reveal global and local structure of similarity between systems (Section 7).
11. Threshold Crossing Events have been manually vetted for additional EB signals resulting in additions to the Catalog.
12. Follow-up data are provided where applicable. This may consist of spectroscopic data (Section 9) or additional follow-up photometric data.

3. CATALOG ADDITIONS

The previous release of the Catalog (Paper II) contained 2165 objects with EB and/or ellipsoidal variable signatures, through the second *Kepler* data release (Q0-Q2). In this release, 2878 objects are identified and analyzed from the entire data set of the primary *Kepler* mission (Q0-Q17). All transit events were identified by the main *Kepler* pipeline (Jenkins 2002; Jenkins et al. 2010) and through the following sources explained here.

3.1. Rejected KOI Planet Candidates

The catalog of KOIs (Mullally et al. 2015) provides a list of detected planets and planet candidates. There is an inevitable overlap in attributing transit events to planets, severely diluted binaries, low mass stellar companions, or grazing EBs. As part of the *Kepler* working group efforts, these targets are vetted for any EB-like signature, such as depth changes between successive eclipses (the so-called even–odd culling), detection of a secondary eclipse that is deeper than what would be expected for an $R < 2R_{\rm Jup}$ planet transit (occultation culling), hot white dwarf transits (Rowe et al. 2010; white dwarf culling), spectroscopic follow-up where large amplitudes or double-lined spectra are detected (follow-up culling), and automated vetting programs known as "robovetters" (J. Coughlin et al. 2016, in preparation). High-resolution direct imaging (AO and speckle) and photo-center centroid shifts also indicate the presence of background EBs. These systems can be found in the online *Kepler* EB catalog by searching the "KOI" flag.

3.2. EBF

The EBF (Parvizi et al. 2014) is a fully automated, adaptive, end-to-end computational pipeline used to classify EB light curves. It validates EBs through an independent neural network classification process. The EBF uses a modular approach to process large volumes of data into patterns for recognition by the artificial neural network. This is designed to allow archival data from time-series photometric surveys to be direct input, where each module's parameters are tunable to the characteristics of the input data (e.g., photometric precision, data collection cadence, flux measurement uncertainty) and define

the output options to produce the probability that each individual system is an EB. A complete description can be found in Stassun et al. (2013). The neural network described here was trained on previous releases of this Catalog. The EBF identified 68 systems from Quarter 3 data. Out of the 68 systems submitted to our pipeline only 13 were validated and added to the Catalog.

3.3. Planet Hunters

Planet Hunters is a citizen science project (Fischer et al. 2012) that makes use of the Zooniverse toolset (Lintott et al. 2008) to serve flux-corrected light curves from the *Kepler* public release data. This process is done manually by visual inspection of each light curve for transit events. For a complete description of the process see Fischer et al. (2012). Identified transit events not planetary in nature are submitted to our pipeline for further vetting and addition to the Catalog.

3.4. Increased Baseline Revisions

An increased timespan allows the ephemerides for all EB candidates to be determined to a greater precision. All ephemerides have been manually vetted, but for certain systems it was impossible to uniquely determine the periods, i.e., for systems with equal depth eclipses (versus a single eclipse at half-period). To aid in this process we computed periodograms using three methods: Lomb–Scargle (Lomb 1976; Scargle 1982), Analysis of Variance (Schwarzenberg-Czerny 1989), and Box-fitting Least Squares (BLS) (Kovács et al. 2002), as implemented in the vartools package (Hartman 2012). Systems with equal depth eclipses may be revised in the future with additional follow-up data (Section 9).

3.5. Period and Ephemeris Error Estimates

We now provide error estimates on both the period and time of eclipse (BJD_0) for every EB in the catalog. The period error is determined through an adaptation of the Period Error Calculator algorithm of Mighell & Plavchan (2013). Using error propagation theory, the period error is calculated from the following parameters: timing uncertainty for a measured flux value, the total length of the time series, the period of the variable, and the maximum number of periods that can occur in the time series.

To revise a precise value and estimate the uncertainty on BJD_0, we use the eclipse bisectors. The bisectors work by shifting the BJD_0 until the left and the right eclipse sides of the phased data overlap as much as possible. The overlap function is fitted by a Gaussian, where the mean is the BJD_0 estimate, and the width is the corresponding error. For those in which this estimates an error larger than the measured width of the eclipse, generally due to extremely low signal to noise, we assume the width of the eclipse as the error instead. Since there is not a well defined BJD_0 for binary heartbeat stars that do not exhibit an actual eclipse in the light curve, we do not estimate or provide uncertainties for these objects.

4. CATALOG DELETIONS

In order to provide the EB community with the most accurate information, we checked each of the 2878 systems against extrinsic variability (i.e., third light contamination, cross talk, and other instrumental artifacts). We generated
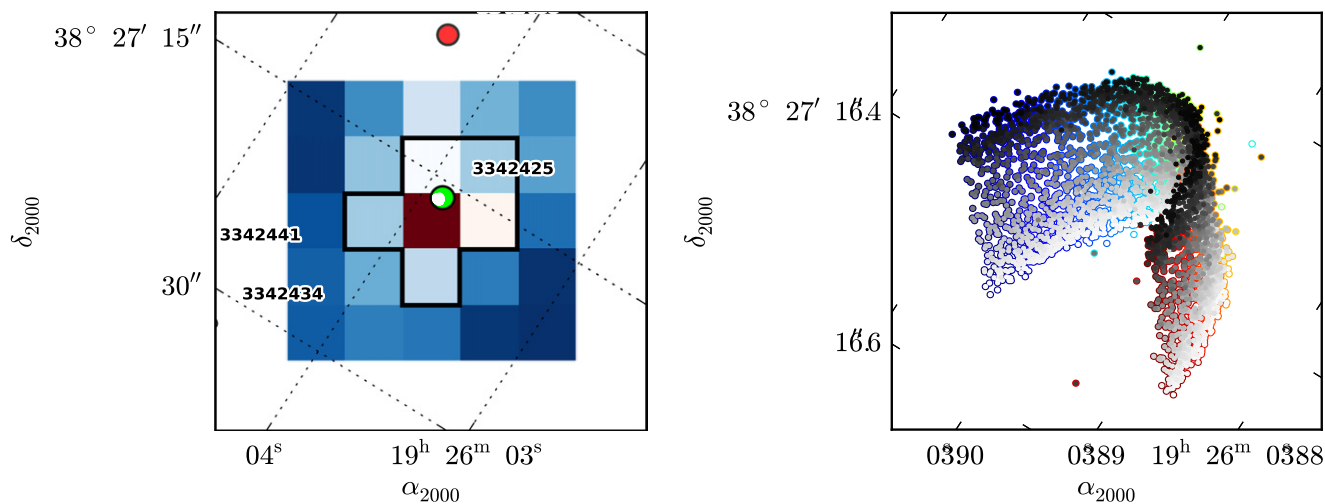
Figure 1. Diagnostic plots for one quarter. In this example the target in question (KIC 3342425) is responsible for the binary signal. In the left-hand plot we see that the pixel contributing the most flux is under the target. On the right-hand side we observe the centroid movement in time. The dispersion in the *y*-direction (for this particular system) is due to the target eclipsing, causing the flux to decrease and the centroid to migrate toward the brighter star, which can be seen in the upper part of the left-hand plot.
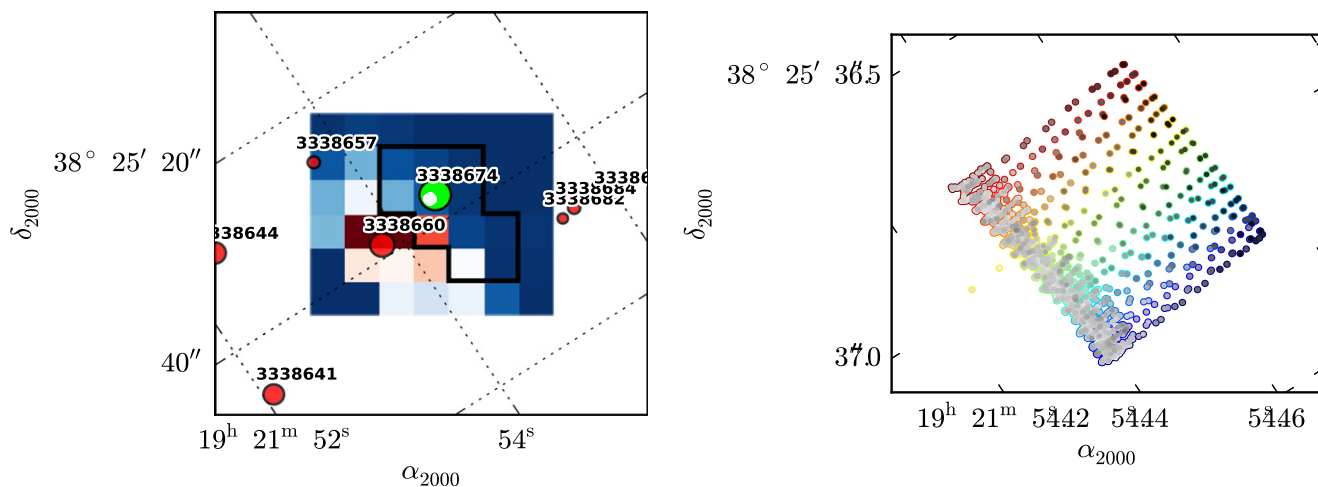
Figure 2. Diagnostic plots for one quarter. In this example the target in question (KIC 3338674) is not responsible for the binary signal seen. On the left-hand side we see that the pixels contributing the most signal are not associated with our target. On the right-hand side we see that the centroid is constantly pulled elsewhere while only returning to our target when the off-target star is in eclipse. The binary light curve is generated by KIC 3338660, making KIC 3338674 a false positive.

diagnostic plots for each available quarter of data for every object in the *Kepler* EB catalog to confirm whether the target was the true source of the EB signal; if the target was not the source of the signal it was deemed a FP.

To do this, we design and generate two diagnostic plots per quarter that—when considered together with all other data— give insight into which object in the TPF map is responsible for the binary signal observed in the light curve. Figures 1 and 2 show a heat map (left panels) that depicts the correlation of the eclipse depth of each individual pixel within the *Kepler* aperture (outlined in black) compared to the eclipse depth of the summed light curves of all the pixels in the aperture. The color scale of the heat map is normalized to the summed *Kepler* light curve divided by the number of pixels in the aperture; the average of pixels in the mask is assigned to white. The heat map shows where the signal contribution is located. Red colors represent pixels with a higher signal contribution while blue colors represent pixels with a lower signal contribution than the average-value pixels. A green circle represents the target KIC that is being processed while any other KIC objects in the

frame are plotted with red circles. The coordinates of these circles come from KIC catalog positions. The radius of the circles correspond to the *Kepler* magnitude. The collection of white dots, typically located near the green circle, represent the location and shape of the centroid. The centroid is the center of light in the pixel window at a given time during the quarter.

The second diagnostic plot (Figures 1 and 2, right panels) illustrates an expanded view of the centroid movement throughout a given quarter. The varying colors of each circle edge represent the transition in time from the beginning of the quarter (blue) to the end of the quarter (red). The gray-scale color of each circle represents the detrended flux of the light curve at that moment, with darker shades representing lower flux. As the binary eclipses, the flux decreases and the centroid migrates toward areas of higher flux (typically away from the binary source). This, in conjunction with the heat map, gives insight into which object is responsible for the binary activity.

These diagnostic plots, in conjunction with other data, were analyzed and EB Working Group members voted on which object in the window was responsible for the binary signal.
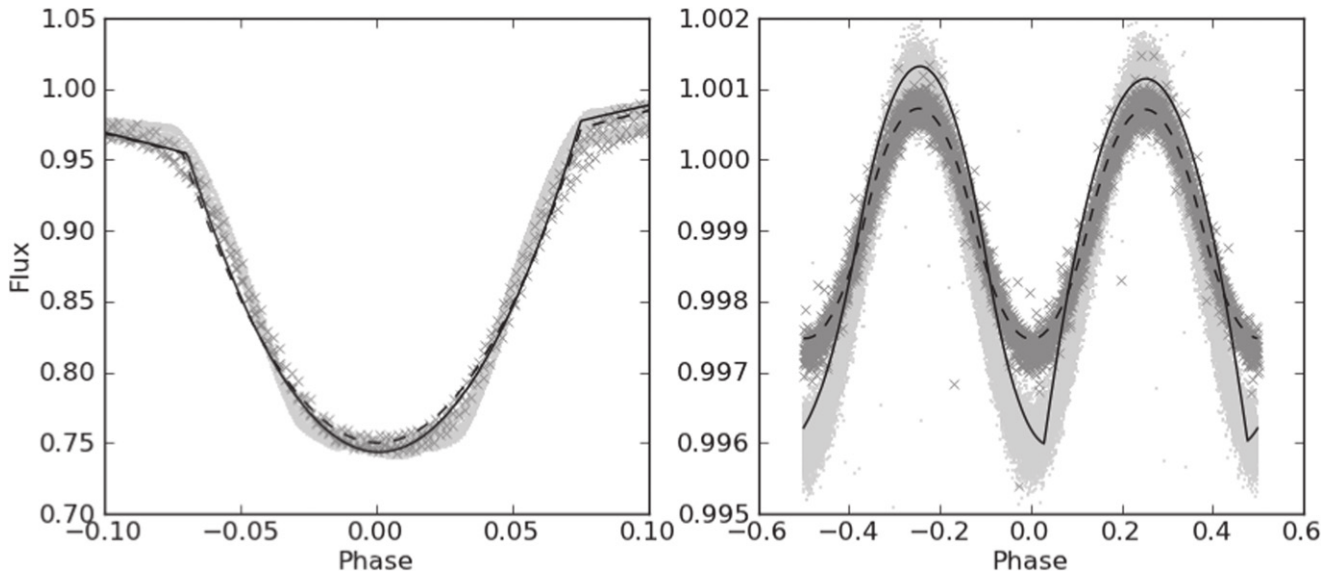
Figure 3. Original polyfit (dashed line) and deconvolved polyfit (solid line) plotted on top of short-cadence (light dots) and long-cadence (darker *x*) Q2 data of KIC 11560447 and 6947064. In both cases, the deconvolution was successful in finding a polyfit which when convolved best fits the long-cadence data, but this does not necessarily fit the short-cadence data or make physical sense.

This was a blind vote with the results tabulated continuously. If the decision was not unanimous the targets were discussed in open group sessions using additional resources from data validation (DV) disposition reports (Coughlin et al. 2014) when available at NExScI.[37]

In addition to checking extrinsic variability, ephemeris cross-matching was performed across the Catalog to identify more FPs. This cross-matching solved ambiguity between double and half-period systems (for systems whose primary and secondary shape are identical). Any matches found this way were manually inspected to identify the true source and remove the FP.

5. LIGHT CURVE DECONVOLUTION

Due to *Kepler*'s long-cadence 30 minute exposure, the phased light curves suffer from a convolution effect. For short-period binaries this phase-dependent smoothing can have a significant impact on the overall shape of the polyfit representation, which would then propagate through the remaining steps of the pipeline. To mitigate this effect, we deconvolve the original polyfit that was determined from the phased long-cadence data. Since there are an infinite number of functions that would convolve to the original polyfit, we impose that the deconvolved representation must also be described by a polyfit. This does not necessarily guarantee a unique solution, but does add the constraint that the deconvolved curve resembles the signal from a binary. We start with the original polyfit and use a downhill simplex algorithm to adjust the various coefficients and knots, minimizing the residuals between the original polyfit and the convolved candidate-polyfit. This process results in another polyfit that, when convolved with a 30 minute boxcar, most closely resembles the original polyfit and, therefore, the phased long-cadence data (Figure 3). This results in a better representation of the actual light curve of the binary which

can then be used to estimate geometrical properties of the binary.

Kepler's short-cadence photometry (1 minute exposures) is short enough that the convolution effect is negligible. However, short cadence data are not available for all systems. Thus, to stay internally consistent, we use only long-cadence data to determine physical parameters and ETVs. Nevertheless, short-cadence data allow us to confirm the effect of convolution and test the performance of our deconvolution process. Comparing the deconvolved polyfit with the short-cadence data from the same EB shows that deconvolution is essential for more accurate approximations but can also result in a representation that does not make physical sense (see the right panel in 3). For this reason, if the deconvolved polyfit for a short-period EB looks suspicious, the deconvolution process likely introduced undesired artifacts into the light curve representation.

6. CLASSIFICATION OF LIGHT CURVES

EB light curves come in a variety of different shapes that are governed by a number of parameters. In order to overcome the drawbacks of manual classification, we performed an automated classification of all identified EB light curves with a general dimensionality reduction numerical tool called LLE (Roweis & Saul 2000). This method is able to project a high-dimensional data set onto a much lower-dimensional manifold in such a way that it retains the local properties of the original data set, so all light curves that are placed close together in the original space are also nearby each other in the projected space (Paper III). This way the relations between the light curves are much easier to investigate. The input space is represented by a collection of polyfit models corresponding to each of the EB light curves in the Catalog. All polyfits were calculated in 1000 equidistant phase points (representing the original space) and then projected to a two-dimensional space, resulting in an arc-shaped manifold. Inspection of the underlying light curves along the arc revealed that one end of the arc was populated by well-detached binaries while the other hosted the overcontact binaries and systems with ellipsoidal variations. Semi-detached

---

systems were in the middle. We assigned a single number to each of the light curves based on where on the arc their projection is located to provide an easy-to-use single-number quantitative representation of the light curves. Values of the parameter range from 0 to 0.1 for well-detached systems, values below 0.5 predominantly belong to detached systems and between 0.5 and 0.7 to semi-detached systems. Over-contact systems usually have values between 0.7 and 0.8, while even higher values up to 1 usually belong to ellipsoidal variables.

In addition to the classification number, we also provide the depths and widths of the primary and secondary eclipses, as well as the separations between eclipses from the polyfit. Depths are determined from the amplitude of the polynomial fitted to the eclipse and are in units of normalized flux. A depth measurement is provided so long as it is larger than three times the estimated scatter of the light curve baseline. For this reason, values are not provided for a secondary eclipse if the signal to noise is not sufficient. Widths are determined by the "knots" connecting the individual polynomial sections and are in units of phase. Separations are determined as the distance between the primary and secondary minimum, also in units of phase, and are defined to always be less than or equal to 0.5. These values are only approximate measures and are only as accurate as the polyfits themselves. Nevertheless, they do provide some measure of the signal-to-noise and also allow for an estimate of eccentricities (Prša et al. 2015).

7. VISUALIZING *KEPLER* DATA

Visualization is an important aspect of data mining—it allows a more intuitive and interactive approach to analyzing and interpreting the data set. The employed algorithm, t-Distributed Stochastic Neighbor Embedding (t-SNE; Maaten & Hinton 2008) is particularly useful for high-dimensional data that lie on several different, but related, lower-dimensional manifolds. It allows the user to simultaneously view EB properties from multiple viewpoints.

7.1. The t-SNE Algorithm

An extension to the EB classification with LLE has been performed using a new technique of visualizing high-dimensional data, first proposed and developed by Maaten & Hinton (2008). This technique, called t-SNE, is a modified version of the Stochastic Neighbor Embedding technique and has a specific appeal for visualizing data, since it is capable of revealing both global and local structure in terms of clustering data with respect to similarity. We provide a brief overview of the basic principles of the t-SNE technique, the results of its application to *Kepler* data and its implementation in the interactive visualization of the Catalog.

Stochastic Neighbor Embedding defines data similarities in terms of conditional probabilities in the high-dimensional data space and their low-dimensional projection. Neighbors of a data-point in the high-dimensional data space are picked in proportion to their probability density under a Gaussian. Therefore, the similarity of two data-points is equivalent to a conditional probability. In t-SNE, the conditional probability is replaced by a joint probability that depends upon the number of data-points. This ensures that all data-points contribute to the cost function by a significant amount, including the outliers. The conditional probability of the corresponding low-dimensional counterparts in SNE is also defined in terms of a Gaussian probability distribution, but t-SNE has introduced a symmetrized Student t-distribution, which leads to joint probabilities of the map. This allows for a higher dispersion of data-points in the low-dimensional map and avoids unwanted attractive forces, since a moderate distance in the high-dimensional map can be represented well by larger distances in its low-dimensional counterpart.

An input parameter that defines the configuration of the output map is the so-called perplexity. Therefore, instead of providing the desired number of nearest neighbors, the user provides a desired value of the perplexity and leaves it up to the method to determine the number of nearest neighbors, based on the data density. This in turn means that the data itself affects the number of nearest neighbors, which might vary from point to point.

7.2. t-SNE and Kepler Data

We have applied t-SNE to various samples of *Kepler* data and compared the results to other methods (LLE, manual flags). We have also attempted two different approaches to the two-dimensional projection: one with direct high-dimensional to two-dimensional mapping and one equivalent to the LLE classification method already implemented in the Catalog (Paper III), where the high-dimensional data space is first mapped to a 3D projection, and subsequently mapped to a 2D projection. The latter approach performs better in terms of clustering data-points and reveals a lumpier data structure, while the first approach results in a rather continuous structure, which might render a more elegant visualization of certain parameter distributions over the projection.

Both the two-step and the direct projection seem to be in agreement with the results obtained with LLE. One advantage of LLE over t-SNE is its simple structure, which allowed for a quantitative classification in terms of the morphology parameter (Paper III). The complex two-dimensional structure of the t-SNE projection makes that task substantially more difficult, so we use t-SNE only as a visualization tool, and retain LLE for classification.

The distribution of the LLE morphology parameter on the t-SNE projection is depicted in Figure 4. The concordance between the two methods is evident from the continuous variation of the morphology parameter along the map. It also serves to further illustrate the performance of t-SNE in terms of large-scale and small-scale structure. For example, the two islands in the right corner of the two-step projection (Figure 4, panel (a)), which incorporate mainly noisy and unique light curve data, still manage to retain the large-scale gradient of the morphology parameter directed from the bottom to the top of the projection.

Further comparison also shows the two-step t-SNE ability to distinguish the main types of EBs: objects with a morphology parameter c (Paper III) $\lesssim 0.4$, corresponding to detached binaries, are a separate cluster from those with $0.4 \lesssim c \lesssim 0.8$ and those with $0.7 \lesssim c \lesssim 0.8$. Those with $c \gtrsim 0.8$, corresponding to ellipsoidal variations and objects with uncertain classification, are grouped into the topmost cluster, separate from all the previous ones. Based on this, it is safe to conclude that t-SNE also performs in line with the manual classification and it might be useful in speeding up or even replacing the subjective manual classification process.
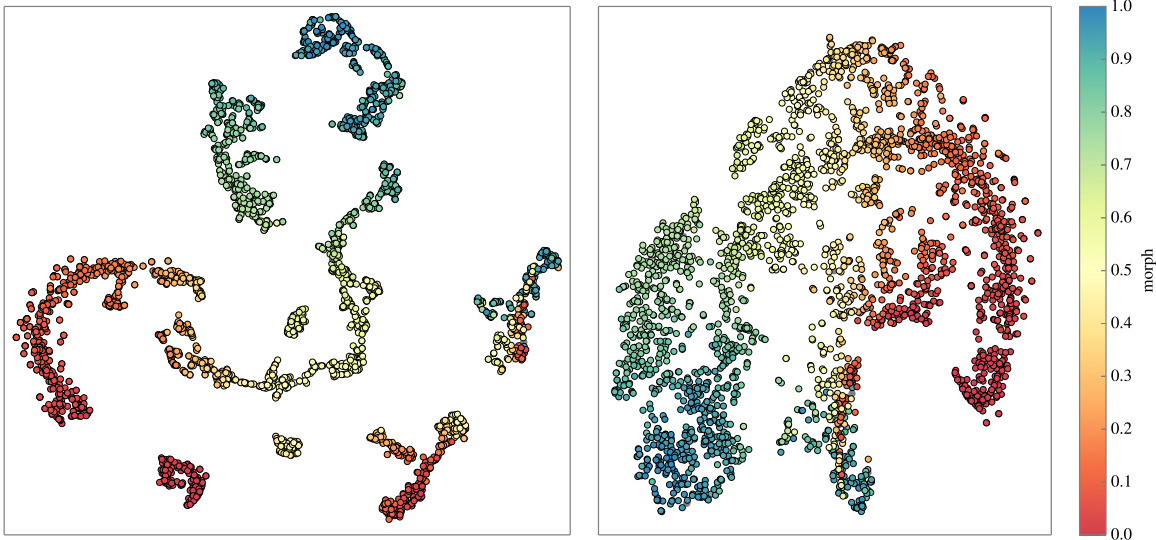
Figure 4. Distribution of the LLE morphology parameter over the two-step (panel (a)) and direct 2D t-SNE projection (panel (b)).

To further illustrate the performance of the technique, we have generated plots of all cataloged parameters over the projection. In all cases the distribution seems fairly smooth, which attests to the broad range of technique applicability. Plots of the distribution of primary eclipse width and secondary eclipse depth obtained with polyfit, and the ratio of temperatures ($T2/T1$) and $\sin i$ obtained through geometric analysis, are provided in Figure 5 (panels (a)–(d) respectively).

An example of the power of tSNE to reveal substructure and distinguish between many different types of similarities which may arise from parameters such as inclination, primary eclipse widths, secondary eclipse depth etc., within a given classification can be seen in the "branches" of Figure 4 (panel (b)) and revealed in Figure 5. The two groups of light curves corresponding to ellipsoidal variations ($c \gtrsim 0.8$) at the bottom of Figure 4 (panel (b)) are especially indicative of this, since only the left branch corresponds to manually classified ellipsoidal light curves, while the right branch, although having a morph parameter that corresponds to ellipsoidal curves, is in fact composed of noisy or unique light curves that can not be classified into any of the primary morphological types. Most of the heartbeat stars can be found at the bottom of this branch.

To fully benefit from the capabilities of the technique, we implemented an interactive version in the Catalog, which combines the t-SNE visualization of *Kepler* data with a broad range of parameter distributions. This extends the data possibilities to a more intuitive and interactive approach, enabling the user to directly view the properties of certain light curves with respect to the whole Catalog. This can be found at http://keplerEBs.villanova.edu/tsne.

8. INTERESTING CLASSES OF OBJECTS IN THE CATALOG

8.1. Heartbeat Stars

Heartbeat stars are a subclass of eccentric ellipsoidal variables introduced by Thompson et al. (2012). The most prominent feature in the heartbeat star light curve is the increased brightness at periastron (where periastron is defined as the closest approach of the two binary star components) caused by stellar deformation, which is a consequence of gravitational interactions; and heating (Figure 6). The morphology of the heartbeat-star light curve defines the heartbeat star—a periastron variation preceded and succeeded by a flat region (ignoring pulsations and spots etc.). As shown by Kumar et al. (1995), the shape of the brightening primarily depends on three orbital properties: argument of periastron, eccentricity, and inclination. This is true for the majority of objects where irradiation effects cause only minor modifications (Burkart et al. 2012). However, this effect is temperature dependent and so for objects with hotter components that both contribute significantly to the flux, as in the case of KOI-54 (Welsh et al. 2011), which contains two A stars, the irradiation contributes notably to the light curve (approximately half of the amplitude of the periastron variation of KOI-54 is a consequence of irradiation). Overall, the amplitude of the periastron brightening depends on the temperature and structure of the stellar components, and the periastron distance. This enables heartbeat stars to be modeled without the presence of eclipses and thus at any inclination. Table 1 contains the *Kepler* catalog identifiers (KIC) and corresponding periods for 173 currently known heartbeat stars in the *Kepler* sample. These systems are flagged with the "HB" flag in the Catalog.

As the stellar components are in close proximity at periastron (relative to their radii), they are subject to strongly varying gravitational forces. Consequently, the stars experience large torques during periastron flybys, making them likely candidates for apsidal motion: the precession of the line of apsides about the center of mass (Claret & Gimenez 1993). Since apsidal motion changes the argument of periastron, the advance can be determined by the change in the shape of the heartbeat light curve, assuming that the data set is long enough for the change to be detected. Figure 7 shows an example of how the light curve of a heartbeat star changes as a function of the argument of periastron for the case of KIC 3749404, which exhibits one of the largest periastron advance rates of $\sim 2^\circ$ yr^{-1}. The central density of the stellar components can be empirically inferred through the rate of the apsidal advance (Claret & Giménez 2010), enabling us to test our current understanding of stellar structure and evolution. Furthermore, as approximately half of all the known *Kepler* heartbeat stars have periods $3 < P < 15$ days and high eccentricities ($e > 0.3$), heartbeat
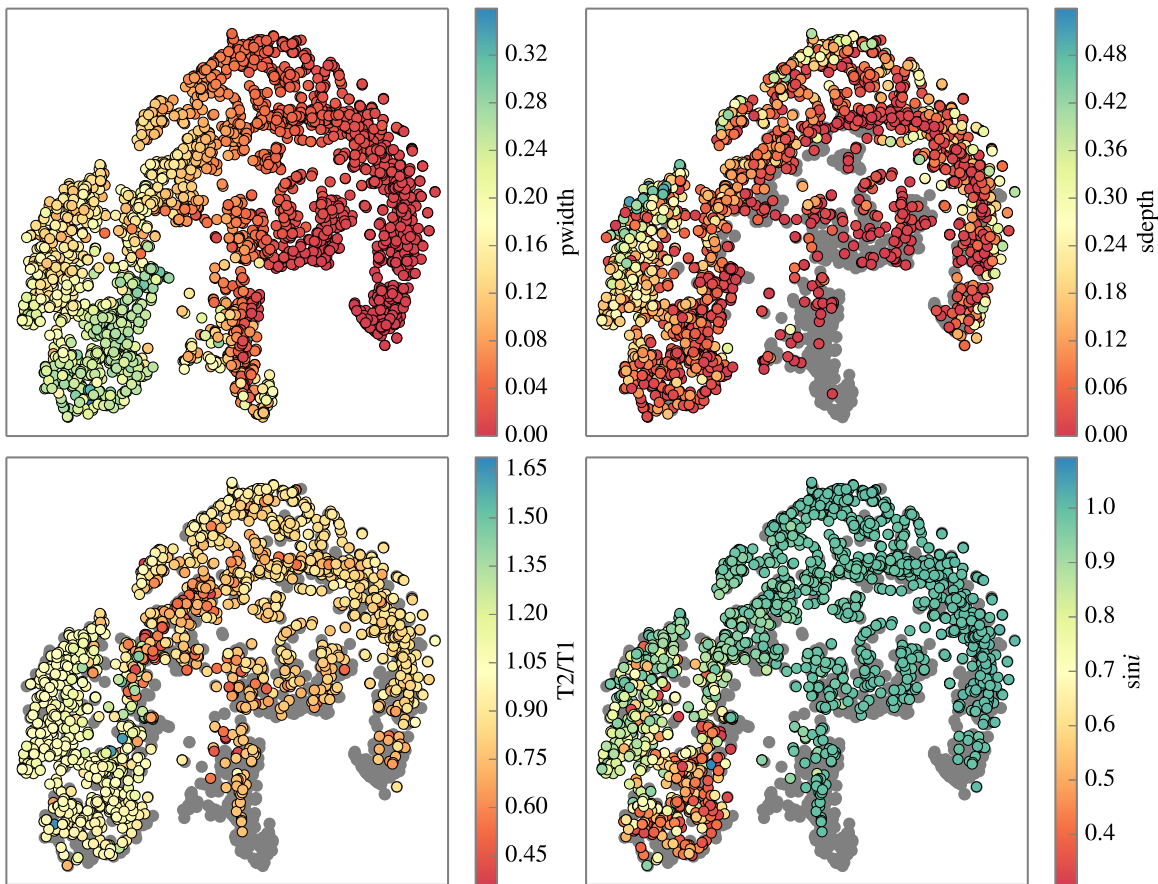
Figure 5. Distribution of primary eclipse width (panel (a)), secondary eclipse depth (panel (b)), $T2/T1$ (panel (c)) and $\sin i$ (panel (d)) parameters over the direct 2D t-SNE projection. The data points that do not have a value for the desired parameter are marked in gray.

stars are ideal for testing theories on relativistic apsidal motion (Gimenez 1985).

8.1.1. Tidally Induced Pulsations

Approximately 15% of these interesting objects also demonstrate tidally induced pulsations, e.g., HD174884 (Maceroni et al. 2009), HD177863 (Willems & Aerts 2002), KOI-54 (Welsh et al. 2011; Burkart et al. 2012; Fuller & Lai 2012), and KIC 4544587 (Hambleton et al. 2013). The signature of a tidally induced pulsation is a mode (or modes) that is an integer multiple of the orbital frequency. From our sample, the record holder, KIC 8164262, has a tidally induced pulsation amplitude of 1 mmag. The majority of objects in our sample have tidally induced pulsations with maximum amplitudes of ~0.1 mmag. Tidally induced modes occur when the orbital frequency is close to an eigenfrequency of the stellar component, causing the star to act like a forced oscillator, which significantly increases the amplitude of the mode. Zahn (1975) hypothesized the existence of tidally induced pulsations as a mechanism for the circularization of binary orbits, attributed to the exchange of orbital angular momentum and loss of orbital energy through mode damping. The high occurrence rate of tidally induced pulsations in heartbeat stars is due to their eccentric nature and small periastron distances leading to interaction times that are comparable to the eigenmodes of the stellar components. The right panel of Figure 6 shows a selection of heartbeat star light curves folded on their orbital periods. The stellar pulsations are clearly visible

as they are exact integer multiples of the orbital frequency: the signature of tidally induced pulsations. These 24 systems are flagged with the "TP" flag.

8.2. Reflection Effect Binaries

The reflection effect is the mutual irradiation of the facing hemispheres of two stars in the binary system. This irradiation alters the temperature structure in the atmosphere of the star, resulting in an increased intensity and flux. This effect reveals itself with an increased flux level on the ingress and egress of the eclipse in the light curve. There are currently 36 of these systems (Table 3). These systems are flagged with the "REF" flag.

8.3. Occultation Pairs

The majority of the stars that make up the Milky Way galaxy are M-type stars and, since they are faint because of their low mass, luminosity, and temperature, the only direct way to measure their masses and radii is by analyzing their light curves in EBs. An issue in the theory of these low-mass stars is the discrepancy between predicted and observed radii of M-type stars (Feiden 2015). When these stars are found in binaries with an earlier type component, the ratio in radii is quite large, and eclipses are total and occulting. Other extreme radius ratio pairs produce similar light curves, such as white dwarfs and main sequence stars, or main sequence stars and giants. Irrespective of the underlying morphology, these occultation pairs are
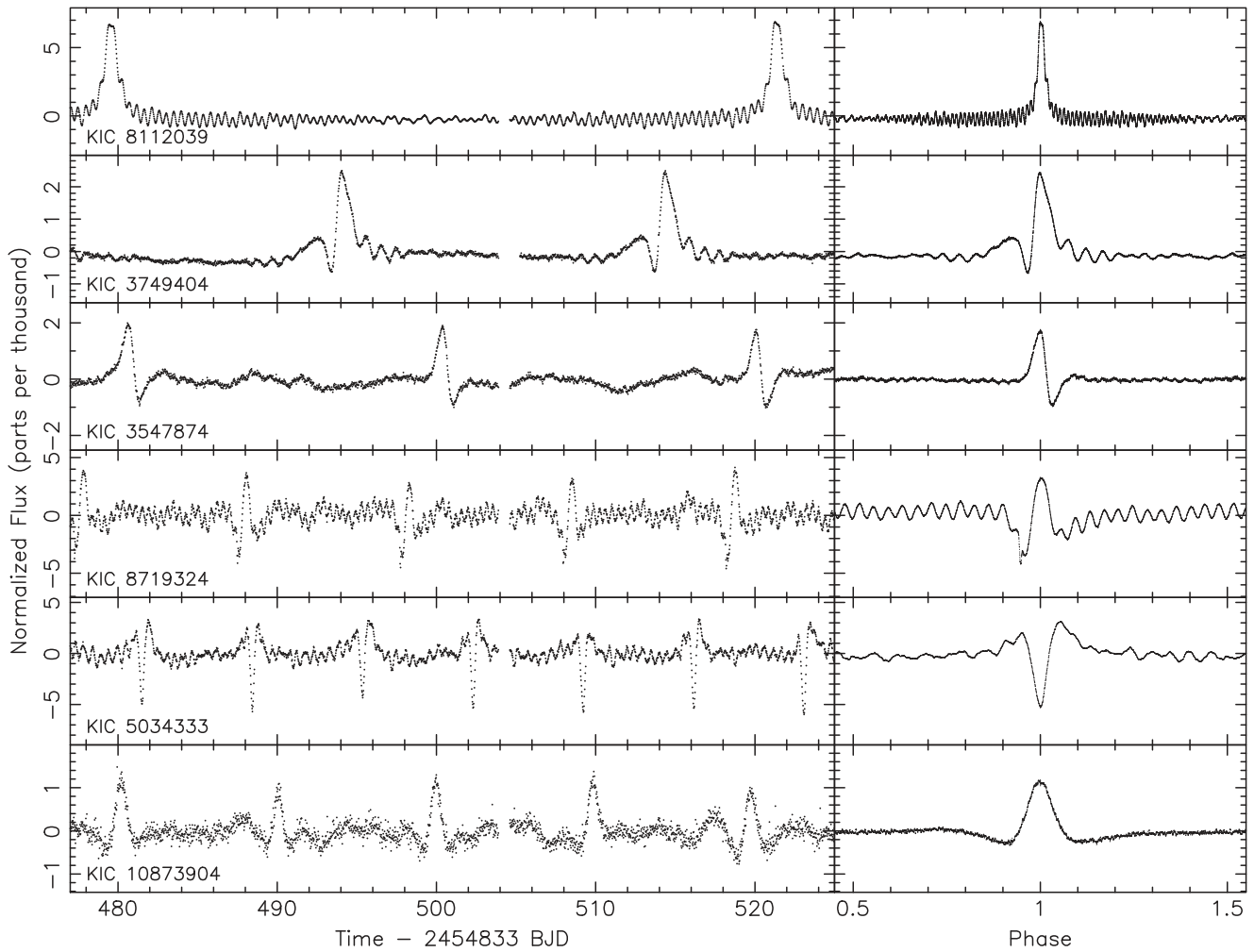
Figure 6. Time series of a selection of *Kepler* heartbeat star light curves (left panel) and phase folded data (right panel). The phase folded data clearly depict the oscillations that are integer multiples of the orbital frequency: tidally induced pulsations. It is worth noting that KIC 8112039 is KOI 54 (Welsh et al. 2011).

critical gauges because eclipses are total and the models are thus additionally constrained.

There are currently 32 of these systems (Table 4). These systems are flagged with the "OCC" flag.

8.4. Circumbinary Planets

The search for circumbinary planets in the *Kepler* data includes looking for transits with multiple features (Deeg et al. 1998; Doyle et al. 2000). Transit patterns with multiple features are caused by a slowly moving object crossing in front of the EB; it is alternately silhouetted by the motion of the background binary stars as they orbit about each other producing predictable but non-periodic features of various shapes and depths. Emerging trends from studying these circumbinary planet systems show the planets orbital plane very close to the plane of the binary (in prograde motion) in addition to the host star. The orbits of the planets are in close proximity to the critical radius and the planet's sizes (in mass and/or radius) are smaller than that of Jupiter. A full discussion of these trends can be found in Welsh et al. (2014). There are currently 14 of these systems (Table 5). These systems are flagged with the "CBP" flag.

8.5. Targets with Multiple Ephemerides

Sources with additional features (8.4) can be another sign of a stellar triple or multiple system (in addition to ETV signals described in Orosz 2015 and J. Orosz et al. 2016, in preparation). In this case the depth of the event is too deep to be the transit of a planet but is instead an eclipse by, or occultation of a third stellar body. A well known example is described in Carter et al. (2011). We have been looking for such features in the Catalog and have uncovered 14 systems exhibiting multiple, determinable periods (Table 6). These systems are flagged with the "M" flag in the Catalog. In some systems, extraneous events are observed whose ephemerides cannot be determined. In some cases the period is longer than the time baseline and two subsequent events have not been observed by *Kepler*. In other cases, eclipsing the inner-binary at different phases results in a nonlinear ephemeris with an indeterminable period. It is worth noting that without spectroscopy or ETVs that are in agreement that additional eclipse event is indeed related, these cases are not guaranteed to be multiple objects—some could be the blend of two independent binaries on the same pixel. These events and their properties are reported in Table 7.

Table 1
The Heartbeat Stars in the *Kepler* Sample

KIC	Period (days)	R.A.(°) (J2000)	Decl.(°) (J2000)
1573836	3.557093	291.5025	37.1775
2010607	18.632296	290.5056	37.4590
2444348	103.206989	291.6687	37.7041
2697935	21.513359	287.4679	37.9666
2720096	26.674680	292.9791	37.9109
3230227	7.047106	290.1126	38.3999
3240976	15.238869	292.9291	38.3280
3547874	19.692172	292.2829	38.6657
3729724	16.418755	285.6555	38.8505
3734660	19.942137	287.6238	38.8554
3749404	20.306385	292.0795	38.8371
3764714	6.633276	295.7400	38.8623
3766353	2.666965	296.0538	38.8943
3850086	19.114247	291.3975	38.9647
3862171	6.996461	294.4970	38.9801
3869825	4.800656	296.1339	38.9990
3965556	6.556770	294.3909	39.0767
4142768	27.991603	287.2629	39.2600
4150136	9.478402	289.6193	39.2939
4247092	21.056416	286.8797	39.3784
4248941	8.644598	287.6032	39.3977
4253860	155.061112	289.2337	39.3865
4359851	13.542328	290.0829	39.4008
4372379	4.535171	293.5203	39.4478
4377638	2.821875	294.7438	39.4994
4450976	12.044869	287.3733	39.5261
4459068	24.955995	290.0244	39.5634
4470124	11.438984	293.1966	39.5072
4545729	18.383520	286.4008	39.6984
4649305	22.651138	290.1033	39.7816
4659476	58.996374	293.1102	39.7564
4669402	8.496468	295.5339	39.7623
4761060	3.361391	295.5471	39.8618
4847343	11.416917	294.9517	39.9294
4847369	12.350014	294.9584	39.9046
4936180	4.640922	295.1137	40.0712
4949187	11.977392	297.9250	40.0884
4949194	41.263202	297.9279	40.0549
5006817	94.811969	290.4560	40.1457
5017127	20.006404	293.5486	40.1117
5034333	6.932280	297.4004	40.1495
5039392	236.727941	298.4009	40.1722
5090937	8.800693	289.2657	40.2555
5129777	26.158530	299.0478	40.2189
5175668	21.882115	288.3171	40.3280
5213466	2.819311	298.1299	40.3999
5284262	17.963312	294.4163	40.4802
5286221	15.295983	294.9404	40.4966
5398002	14.153175	300.0150	40.5270
5511076	6.513199	282.9722	40.7270
5596440	10.474857	282.7207	40.8992
5707897	8.416091	292.5603	40.9969
5733154	62.519903	298.6118	40.9491
5736537	1.761529	299.2878	40.9129
5771961	26.066437	284.7599	41.0434
5790807	79.996246	291.7718	41.0981
5818706	14.959941	298.6959	41.0417
5877364	89.648538	292.1599	41.1982
5944240	2.553222	285.9139	41.2916
5960989	50.721534	292.0520	41.2661
6042191	43.390923	291.7434	41.3100
6105491	13.299638	284.9915	41.4333
6117415	19.741625	289.8611	41.4082

Table 1
(Continued)

KIC	Period (days)	R.A.(°) (J2000)	Decl.(°) (J2000)
6137885	12.790099	295.8830	41.4747
6141791	13.659035	296.7550	41.4846
6290740	15.151827	293.6252	41.6615
6292925	13.612220	294.2413	41.6198
6370558	60.316584	293.8644	41.7169
6693555	10.875075	292.4559	42.1372
6775034	10.028547	291.0820	42.2686
6806632	9.469157	298.8907	42.2099
6850665	214.716056	287.7663	42.3227
6881709	6.741116	296.6588	42.3698
6963171	23.308219	295.8099	42.4592
7039026	9.943929	293.4486	42.5866
7041856	4.000669	294.2317	42.5901
7050060	22.044000	296.2551	42.5302
7259722	9.633226	283.1575	42.8904
7293054	671.800000	295.0398	42.8795
7350038	13.829942	287.5149	42.9118
7373255	13.661106	294.8559	42.9372
7431665	281.400000	287.3766	43.0095
7511416	5.590855	286.0600	43.1662
7591456	5.835751	285.6098	43.2055
7622059	10.403262	295.9200	43.2818
7660607	2.763401	281.8825	43.3002
7672068	16.836177	287.8638	43.3042
7799540	60.000000	281.1918	43.5250
7833144	2.247734	295.3246	43.5054
7881722	0.953289	288.2734	43.6977
7887124	32.486427	290.4833	43.6224
7897952	66.991639	294.2019	43.6553
7907688	4.344837	297.0531	43.6438
7914906	8.752907	298.8165	43.6733
7918217	63.929799	299.6020	43.6960
7973970	9.479933	296.3820	43.7489
8027591	24.274432	291.3655	43.8680
8095275	23.007350	290.9708	43.9708
8112039	41.808235	296.5647	43.9476
8123430	11.169990	299.3394	43.9996
8144355	80.514104	281.8770	44.0299
8151107	18.001308	285.5886	44.0477
8164262	87.457170	291.2468	44.0004
8197368	9.087917	300.9348	44.0943
8210370	153.700000	280.7721	44.1887
8242350	6.993556	294.9346	44.1298
8264510	5.686759	300.9686	44.1920
8322564	22.258846	298.7603	44.2662
8328376	4.345967	300.3823	44.2801
8386982	72.259590	298.4551	44.3134
8456774	2.886340	299.7266	44.4091
8456998	7.531511	299.7784	44.4611
8459354	53.557318	300.4068	44.4142
8508485	12.595796	296.4474	44.5586
8688110	374.546000	291.3925	44.8952
8696442	12.360553	294.5535	44.8503
8702921	19.384383	296.6650	44.8531
8703887	14.170980	296.9350	44.8503
8707639	7.785196	297.8877	44.8683
8719324	10.232698	301.1143	44.8258
8803882	89.630216	284.7969	45.0991
8838070	43.362724	298.1911	45.0936
8908102	5.414582	298.8360	45.1165
8912308	20.174443	300.0684	45.1016
9016693	26.368027	289.8839	45.3041
9151763	438.051939	290.6850	45.5684

Table 1
(Continued)

KIC	Period (days)	R.A.(°) (J2000)	Decl.(°) (J2000)
9163796	121.006844	295.3375	45.5048
9408183	49.683544	293.4932	45.9876
9535080	49.645296	295.2635	46.1480
9540226	175.458827	297.0340	46.1985
9596037	33.355613	294.9424	46.2501
9701423	8.607397	287.6039	46.4128
9711769	12.935909	292.4648	46.4918
9717958	67.995354	294.9158	46.4853
9790355	14.565548	298.7419	46.5773
9835416	4.036605	293.6965	46.6205
9899216	10.915849	295.1617	46.7506
9965691	15.683195	297.3268	46.8452
9972385	58.422113	299.2823	46.8988
10004546	19.356914	288.7470	46.9307
10092506	31.041675	297.8457	47.0723
10096019	6.867469	298.8533	47.0828
10159014	8.777397	297.7946	47.1565
10162999	3.429215	298.8757	47.1436
10221886	8.316718	296.8986	47.2816
10334122	37.952857	289.6644	47.4004
10611450	11.652748	296.1244	47.8307
10614012	132.167312	296.9287	47.8830
10664416	25.322174	291.4008	47.9246
10679505	5.675186	296.9342	47.9812
10863286	3.723867	292.7082	48.2070
10873904	9.885633	296.6001	48.2960
11044668	139.450000	297.9449	48.5578
11071278	55.885225	284.4661	48.6553
11122789	3.238154	283.1246	48.7349
11133313	27.400893	289.6666	48.7296
11240948	3.401937	290.1068	48.9034
11288684	22.210063	287.1591	49.0800
11403032	7.631634	291.9279	49.2970
11409673	12.317869	295.1364	49.2733
11494130	18.955414	284.0268	49.4154
11506938	22.574780	291.6465	49.4934
11568428	1.710629	296.1853	49.5568
11568657	13.476046	296.2798	49.5178
11572363	19.027753	297.7151	49.5738
11649962	10.562737	284.5680	49.7795
11700133	6.754017	284.2339	49.8532
11769801	29.708220	295.1429	49.9931
11774013	3.756248	296.8993	49.9163
11859811	22.314148	289.3813	50.1894
11923629	17.973284	296.3860	50.2050
11970288	20.702319	295.2126	50.3169
12255108	9.131526	289.5991	50.9386

Table 2
The Systems With Tidally Induced Pulsations in the *Kepler* Sample

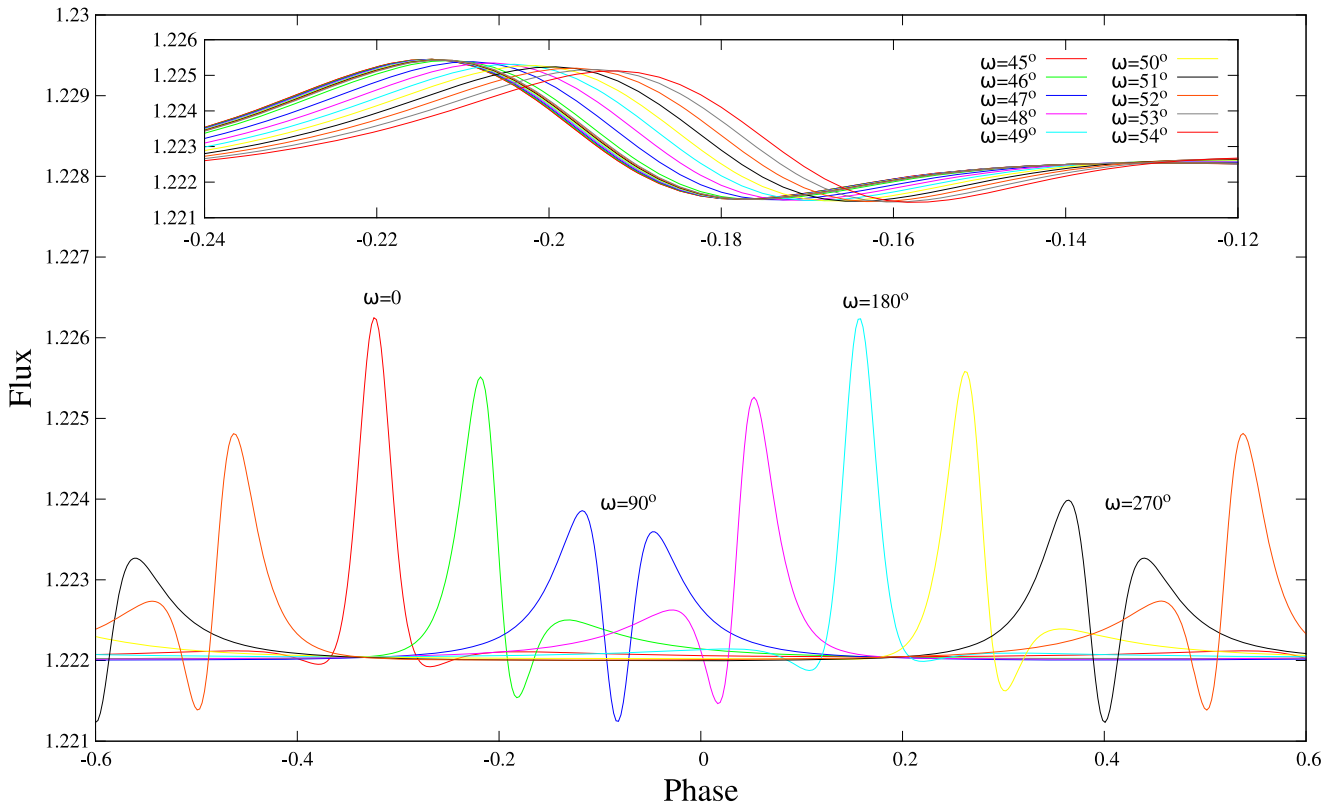| KIC	Period (days)	R.A.(°) (J2000)	Decl.(°) (J2000)
3230227	7.047106	290.1126	38.3999
3547874	19.692172	292.2829	38.6657
3749404	20.306385	292.0795	38.8371
3766353	2.666965	296.0538	38.8943
3869825	4.800656	296.1339	38.9990
4142768	27.991603	287.2629	39.2600
4248941	8.644598	287.6032	39.3977
4949194	41.263202	297.9279	40.0549
5034333	6.932280	297.4004	40.1495
5090937	8.800693	289.2657	40.2555
8095275	23.007350	290.9708	43.9708
8112039	41.808235	296.5647	43.9476
8164262	87.457170	291.2468	44.0004
8264510	5.686759	300.9686	44.1920
8456774	2.886340	299.7266	44.4091
8703887	14.170980	296.9350	44.8503
8719324	10.232698	301.1143	44.8258
9016693	26.368027	289.8839	45.3041
9835416	4.036605	293.6965	46.6205
9899216	10.915849	295.1617	46.7506
11122789	3.238154	283.1246	48.7349
11403032	7.631634	291.9279	49.2970
11409673	12.317869	295.1364	49.2733
11494130	18.955414	284.0268	49.4154

8.7. Eclipse Depth Changes

We have come across 43 systems that exhibit eclipse depth changes (Figure 8). These systems were visually inspected and manually flagged. The depth variations shown here differ from QAM effects; the depth variations are long-term trends spanning multiple, sequential quarters. In 10319590 (see Figure 8), for example, the eclipses actually disappear. Although it is possible that some of these could be caused by gradual aperture movement or a source near the edge of a module leaking light, these variations are not quarter or season-dependent, and are much more likely to actually be physical. Physical causes of these long-term depth variations could include a rapid inclination or periastron change due to the presence of a third body or spot activity as shown in Croll et al. 2015). Table 8 lists these systems and are flagged by the "DV" (Depth Variation) flag.

8.8. Single Eclipse Events

Systems exhibiting a primary and/or secondary eclipse but lack a repeat of either one are shown in Table 9. For these 32 systems no ephemeris, ETV, or period error is determined. These are flagged with the "L" (long) flag and are available from the database under http://keplerEBs.villanova.edu/search but are not included in the EB Catalog.

8.9. Additional Interesting Classes

The Catalog contains many interesting classes of objects which we encourage the community to explore. Some additional classes, which will only be listed (for brevity), include: total eclipsers, occultation binaries, reflection-effect binaries, red giants, pulsators, and short-period detached

8.6. ETVs

In an EB, one normally expects the primary eclipses to be uniformly spaced in time. However, apsidal motion, mass transfer from one star to the other, or the presence of a third body in the system can give rise to changes in the orbital period, which in turn will change the time interval between consecutive eclipse events. These deviations will contain important clues as to the reason for the period change. A table of these systems and more information on their analysis can be found in Conroy et al. (2014) and J. Orosz et al. (2016, in preparation). ETV values and plots are provided for each system in the online Catalog.

Figure 7. Effect of the periastron value, ω, on the shape of the periastron brightening for one full cycle. The peaks change both their position in phase and their shape drastically with varying ω. KIC 3749404 is a heartbeat star that exhibits one of the largest periastron advance rates ($\sim 2° \, \mathrm{yr}^{-1}$; K. Hambleton et al. 2016, in preparation). In the subplot the effect on the light curve over the four year *Kepler* mission is depicted.

systems. These systems can be found using the search criteria provided at http://keplerEBs.villanova.edu/search.

9. SPECTROSCOPIC FOLLOW-UP

Modeling light curves of detached EB stars can only yield relative sizes in binary systems. To obtain the absolute scale, we need RV data. In case of double-lined spectroscopic binaries (SB2), we can obtain the mass ratio q, the projected semimajor axis $a \sin i$ and the center-of-mass (systemic) velocity v_γ. In addition, SB2 RV data also constrain orbital elements, most notably eccentricity e and argument of periastron ω. Using SB2 light curve and RV data in conjunction, we can derive masses and radii of individual components. Using luminosities from light curve data, we can derive distances to these systems. When the luminosity of one star dominates the spectrum, only one RV curve can be extracted from spectra. These are single-lined spectroscopic binaries (SB1), and for those we cannot (generally) obtain a full solution. The light curves of semi-detached and overcontact systems can constrain the absolute scale by way of ellipsoidal variations: continuous flux variations due to the changing projected cross-section of the stars with respect to line of sight as a function of orbital phase. These depend on stellar deformation, which in turn depends on the absolute scale of the system. While possible, the photometric determination of the q and $a \sin i$ is significantly less precise than the SB2 modeling, and the parameter space is plagued by parameter correlations and solution degeneracy. Thus, obtaining spectroscopic data for as many EBs as possible remains a uniquely

important task to obtain the absolute scale and the distances to these systems.

We successfully proposed for 30 nights at the Kitt Peak National Observatory's 4-m telescope to acquire high resolution ($R \geqslant 20{,}000$), moderate signal-to-noise ratio (S/N $\geqslant 15$) spectra using the echelle spectrograph. To maximize the scientific yield given the follow-up time requirement, we prioritized all targets into the following groups:

1. *Well-detached EBs in near-circular orbits.* These are the prime sources for calibrating the *M–L–R–T* relationships across the main sequence. Because of the separation, the components are only marginally distorted and are assumed to have evolved independently from one another. Circular orbits indicate that the ages of these systems are of the order of circularization time (Zahn & Bouchet 1989; Meibom & Mathieu 2005). Modeling these systems with state-of-the-art modeling codes (i.e., WD: Wilson 1979, and its derivatives; ELC: Orosz & Hauschildt 2000; PHOEBE: Prša & Zwitter 2005) that account for a range of physical circumstances allows us to determine their parameters to a very high accuracy. These results can then be used to map the physical properties of these main sequence components to the spectral type determined from spectroscopy. While deconvolution artifacts might raise some concern (see Figure 3 left), in practice they become vanishingly small for orbital periods $\gtrsim$1-day.

2. *Low-mass main sequence EBs.* By combining photometric observations during the eclipses and high-*R* spectroscopy, we can test the long standing discrepancy

Table 3
The Reflection Effect Systems in the *Kepler* Sample

KIC	Period (days)	Period Error (days)	BJD$_0$ (−2400000)	BJD$_0$ Error (days)	R.A.(°) (J2000)	Decl.(°) (J2000)
2708156	1.891272	0.000003	54954.336	0.046	290.2871	37.9365
3339563	0.841232	0.000001	54965.378	0.051	290.7460	38.4431
3431321	1.015049	0.000001	54954.418	0.066	287.7745	38.5040
3547091	3.30558	0.00001	55096.3221	0.0177	292.0785	38.6315
4350454	0.965658	0.000001	54964.943	0.224	287.0525	39.4879
4458989	0.529854	0.000000	54954.1586	0.0337	290.0015	39.5339
5034333	6.93228	0.00002	54954.028	0.054	297.4004	40.1495
5098444	26.9490	0.0001	54984.023	0.082	291.5633	40.2678
5213466	2.81931	0.00001	55165.534	⋯	298.1299	40.3999
5736537	1.76153	0.00001	54965.955	⋯	299.2878	40.9129
5792093	0.600588	0.000000	54964.6434	0.0331	292.2002	41.0137
6262882	0.996501	0.000001	54965.112	0.064	282.6457	41.6087
6387887	0.216900	0.000001	54999.9686	0.0056	298.1854	41.7340
6791604	0.528806	0.000000	54964.6825	0.0284	295.6755	42.2406
7660607	2.76340	0.00001	54954.589	⋯	281.8825	43.3002
7748113	1.734663	0.000002	54954.144	0.102	290.1135	43.4365
7770471	1.15780	0.00000	55000.1826	0.0263	297.1805	43.4771
7833144	2.24773	0.00001	55001.232	⋯	295.3246	43.5054
7881722	0.953289	0.000002	54954.118	⋯	288.2734	43.6977
7884842	1.314548	0.000002	54954.876	0.082	289.6946	43.6260
8455359	2.9637	0.0002	55002.027	0.189	299.3618	44.4112
8758161	0.998218	0.000001	54953.8326	0.0243	293.6205	44.9673
9016693	26.3680	0.0001	55002.583	⋯	289.8839	45.3041
9071373	0.4217690	0.0000003	54953.991	0.109	283.1591	45.4156
9101279	1.811461	0.000003	54965.932	0.047	296.0016	45.4481
9108058	2.1749	0.0001	54999.729	0.049	297.7811	45.4243
9108579	1.169628	0.000001	54954.998	0.069	297.8999	45.4666
9159301	3.04477	0.00001	54956.303	0.063	293.6933	45.5170
9472174	0.1257653	0.0000001	54953.6432	0.0183	294.6359	46.0664
9602595	3.55651	0.00001	54955.853	0.074	297.1435	46.2285
10000490	1.400991	0.000002	54954.2437	0.0286	286.5560	46.9573
10149845	4.05636	0.00001	55001.071	0.237	295.0444	47.1964
10857342	2.41593	0.00003	55005.265	0.056	290.0115	48.2442
11408810	0.749287	0.000001	54953.869	0.047	294.7304	49.2944
12109845	0.865959	0.000003	55000.5582	0.0129	290.9192	50.6964
12216706	1.47106	0.00001	55003.5216	0.0252	295.7438	50.8309

Note. Those reported without BJD$_0$ errors are also heartbeat stars.

between the theoretical and observational mass–radius relations at the bottom of the main-sequence, namely that the observed radii of low-mass stars are up to 15% larger than predicted by structure models. It has been suggested that this discrepancy may be related to strong stellar magnetic fields, which are not properly accounted for in current theoretical models. All previously well-character-ized low-mass main-sequence EBs have periods of a few days or less, and their components are therefore expected to be rotating rapidly as a result of tidal synchronization, thus generating strong magnetic fields. Stars in the binaries with longer orbital periods, which are expected to have weaker magnetic fields, may better match the assumptions of theoretical stellar models. Spectroscopy can provide evidence of stellar chromospheric activity, which is statistically related to ages, thus discriminating between young systems settling onto the main sequence and the older ones already on the main sequence.

3. *EBs featuring total eclipses.* A select few EBs with total eclipses allow us to determine the inclination and the radii to an even higher accuracy, typically a fraction of a

percent. Coupled with RVs, we can obtain the absolute scale of the system and parameters of those systems with unprecedented accuracy.

4. *EBs with intrinsic variations.* Binarity is indiscriminate to spectral and luminosity types. Thus, components can be main-sequence stars, evolved, compact, or intrinsically variable—such as pulsators (δ-Sct, RR Lyr, ...), spots, etc. These components are of prime astrophysical interest to asteroseismology, since we can compare fundamental parameters derived from binarity to those derived from asteroseismic scaling relations (Huber et al. 2014).

5. *EBs exhibiting ETVs.* These variations can be either dynamical or due to the light time effect. The periodic changes of the orbital period are indicative of tertiary components (Conroy et al. 2014). Understanding the frequency of tertiaries in binary systems is crucial because many theories link the third component with the tightening of binary orbits via Kozai–Lidov mechan-ism and/or periastron interactions. Careful studies of statistical properties of ETVs detected in EBs may shed light on the origins of binarity. In addition, the

Table 4
The Occultation Pairs in the *Kepler* Sample

KIC	Period (days)	Period Error (days)	BJD$_0$ (−2400000)	BJD$_0$ Error (days)	R.A.(°) (J2000)	Decl.(°) (J2000)
2445134	8.4120089	0.0000228	54972.648	0.035	291.8497	37.7386
3970233	8.254914	0.000055	54966.160	0.052	295.4819	39.0173
4049124	4.8044707	0.0000102	54969.0039	0.0229	289.3142	39.1314
4386047	2.9006900	0.0000181	55001.2005	0.0253	296.4303	39.4435
4740676	3.4542411	0.0000063	54954.3478	0.0325	289.9644	39.8114
4851464	5.5482571	0.0000159	55005.061	0.046	295.8887	39.9113
5370302	3.9043269	0.0000076	54967.3507	0.0286	294.0568	40.5497
5372966	9.2863571	0.0000262	54967.6753	0.0264	294.7440	40.5339
5728283	6.1982793	0.0000153	55003.981	0.057	297.6203	40.9431
6182019	3.6649654	0.0000074	55003.8010	0.0264	282.6849	41.5880
6362386	4.5924016	0.0000094	54956.954	0.036	291.2642	41.7488
6387450	3.6613261	0.0000069	54968.2691	0.0182	298.0917	41.7941
6694186	5.5542237	0.0000124	54957.0531	0.0325	292.6311	42.1808
6762829	18.795266	0.000072	54971.668	0.079	286.8304	42.2792
7037540	14.405911	0.000063	55294.236	0.044	293.0204	42.5088
7972785	7.3007334	0.0000187	54966.566	0.048	296.0477	43.7621
8230809	4.0783467	0.0000081	54973.317	0.049	290.8917	44.1689
8458207	3.5301622	0.0000065	54967.7749	0.0309	300.0916	44.4148
8460600	6.3520872	0.0000153	54967.2065	0.0286	300.7748	44.4878
8580438	6.4960325	0.0000158	54968.468	0.037	298.3827	44.6156
9048145	8.6678260	0.0000238	54970.3408	0.0331	299.3980	45.3182
9446824	4.2023346	0.0000087	55004.1071	0.0280	282.1844	46.0069
9451127	5.1174021	0.0000111	54967.5858	0.0287	284.8227	46.0137
9649222	5.9186193	0.0000138	54965.9239	0.0285	291.8585	46.3865
9719636	3.351570	0.000044	55000.7919	0.0223	295.5262	46.4571
10020423	7.4483776	0.0000192	54970.6936	0.0289	295.2979	46.9205
10295951	6.8108248	0.0000167	54955.424	0.062	299.1028	47.3778
10710755	4.8166114	0.0000102	54966.7629	0.0271	281.9364	48.0101
11200773	2.4895516	0.0000039	54965.0434	0.0184	296.4774	48.8537
11252617	4.4781198	0.0000096	55006.1732	0.0218	295.6914	48.9038
11404644	5.9025999	0.0000137	54969.388	0.042	292.7561	49.2646
11826400	5.8893723	0.0000135	54956.000	0.037	297.5134	50.0748

Table 5
The Circumbinary Planets in the *Kepler* Sample

KIC	Kepler #	Period (days)	Period Error (days)	R.A.(°) (J2000)	Decl.(°) (J2000)	Citation
12644769	Kepler-16b	41.0776	0.0002	289.075700	51.757400	Doyle et al. (2011)
8572936	Kepler-34b	27.7958	0.0001	296.435800	44.641600	Welsh et al. (2012)
9837578	Kepler-35b	20.7337	0.0001	294.497000	46.689800	Welsh et al. (2012)
6762829	Kepler-38b	18.7953	0.0001	286.830400	42.279200	Orosz et al. (2012b)
10020423	Kepler-47b,c	7.44838	0.00002	295.297900	46.920500	Orosz et al. (2012a)
4862625	Kepler-64b	20.0002	0.0001	298.215100	39.955100	Schwamb et al. (2013)
12351927	Kepler413b	10.11615	0.00003	288.510600	51.162500	Kostov et al. (2014)
9632895	Kepler-453b	27.3220	0.0001	283.241300	46.378500	Welsh et al. (2015)

uncertainty of fundamental parameters derived from multiple stellar systems is an order of magnitude smaller than that of binary stars (Carter et al. 2011; Doyle et al. 2011).

We acquired and reduced multi-epoch spectra for 611 systems within this program; typically 2–3 spectra per target were acquired near the quadratures. The spectra are available for download from the EB Catalog website. Extrapolating from these systems, we anticipate around 30% of the *Kepler* sample of EBs presented in the Catalog to be SB2 systems. The detailed analysis of the acquired spectra is the topic of an upcoming paper (C. Johnston et al. 2016, in preparation).

10. CATALOG ANALYSIS

In Papers I and II we noted a non-uniform distribution of EB occurrence rates as a function of galactic latitude. This was surprising at first, since the implication that EB stars are not uniformly distributed in space is not immediately obvious. Galaxy population observations and models, however, have long predicted this behavior: the stellar population at lower galactic latitudes (thin disk) contains notably younger stars that are on average larger (i.e., contain more giants in the magnitude-limited sample) than the older, sparser population of the thick disk and halo (Prša et al. 2015). In consequence, the geometric probability of eclipses increases toward the

Table 6
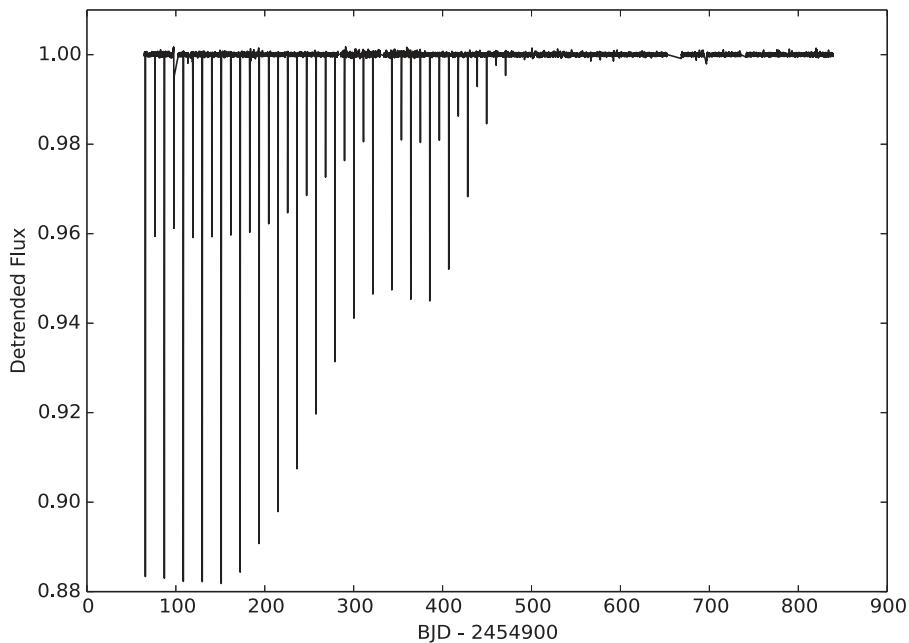The Systems Exhibiting Multiple Ephemerides in the *Kepler* Sample

KIC	Period (days)	Period Error (days)	BJD$_0$ (−2400000)	BJD$_0$ Error (days)	R.A.(°) (J2000)	Decl.(°) (J2000)
2856960	0.2585073	0.0000001	54964.658506	0.007310	292.3813	38.0767
2856960	204.256	0.002	54997.652563	0.369952	292.3813	38.0767
4150611	8.65309	0.00002	54961.005419	0.024746	289.7425	39.2671
4150611	1.522279	0.000002	54999.688801	0.003464	289.7425	39.2671
4150611	94.198	0.001	55029.333888	0.328165	289.7425	39.2671
5255552	32.4486	0.0002	54970.636491	0.116220	284.6931	40.4986
5897826	33.8042	0.0002	54967.628858	0.116761	297.4759	41.1143
5952403	0.905678	0.000001	54965.197892	0.014736	289.2874	41.2648
6665064	0.69837	0.00001	54964.697452	0.009707	281.6500	42.1321
6964043	5.36258	0.00002	55292.008176	0.308696	296.0145	42.4223
7289157	5.26581	0.00001	54969.976049	0.044130	293.9661	42.8373
7289157	242.713	0.002	54996.317389	0.055294	293.9661	42.8373
9007918	1.387207	0.000002	54954.746682	0.023254	286.0084	45.3560
11495766	8.34044	0.00002	55009.377729	0.046025	285.2253	49.4242

Table 7
Properties of the Extraneous Events Found in the *Kepler* Sample

KIC	Event Depth (%)	Event Width (days)	Start Time (−240000)	End Time (240000)
6543674	0.96	2.	55023	55025
7222362	0.6	0.6	55280.9	55281.5
7222362	0.8	2	55307.5	55309.5
7222362	0.65	2	55975.5	55977.5
7668648	0.94	0.2	55501.1	55501.3
7668648	0.94	0.2	55905.5	55905.7
7668648	0.94	0.2	56104.4	56104.6
7668648	0.94	0.2	56303.7	56303.9
7670485	0.975	1.0	55663	55664

galactic disk. Figure 9 depicts this distribution for the complete sample of EBs in the current Catalog. Galactic latitudes are divided into ~1° bins and EBs within those bins are counted. To get the area-corrected occurrence rates, their number is divided by the number of all stars observed by *Kepler* within

the same bins. The latitude-dependent occurrence rate is immediately obvious. To the *j*th bin we assigned a corresponding error of $\sqrt{N_j}/N_{\mathrm{tot},j}$, where N_j is the number of detected EBs and $N_{\mathrm{tot},j}$ is the number of all stars in that bin. Unfortunately, *Kepler*'s latitude span is not sufficient to fit an actual galactic population model to the number of EBs detected, so we resort to a toy proxy using a simple exponential fit: $dp/db(b) = A\exp(-C(b - B)) + D$. We performed a least squares fit to derive parameters of the exponential, depicted by a solid line in Figure 9. This toy model predicts that the largest expected occurrence rate of EBs is $A + D \sim 2.2\%$, while the smallest expected occurrence rate is $D \sim 0.9\%$. Parameter *B* drives the galactic latitude offset ($b \sim 4°$) where the exponential rise of EBs in this magnitude-limited sample is still a reasonable approximation, beyond which the disk opaqueness causes the number of EBs to level off and the exponential model to fail. Finally, parameter *C* provides an estimate of thin-to-thick disk transition, determined predominantly by the decrease in the number of giants in the magnitude-limited sample.

Figure 8. KIC 10319590 is a system undergoing eclipse depth variations.

15

Table 8
The Systems Exhibiting Eclipse Depth Variations in the *Kepler* Sample

KIC	Period (days)	Period Error (days)	BJD$_0$ (−2400000)	BJD$_0$ Error (days)	R.A.(°) (J2000)	Decl.(°) (J2000)
1722276	569.95	0.01	55081.923700	0.035212	291.6967	37.2380
2697935	21.5134	0.0001	55008.469440	...	287.4679	37.9666
2708156	1.891272	0.000003	54954.335595	0.046299	290.2871	37.9365
3247294	67.419	0.000	54966.433454	0.046494	294.4399	38.3808
3867593	73.332	0.000	55042.964810	0.063167	295.6975	38.9020
3936357	0.3691536	0.0000002	54953.852697	0.020054	285.4109	39.0412
4069063	0.504296	0.000000	54964.906342	0.010072	294.5585	39.1377
4769799	21.9293	0.0001	54968.505532	0.061744	297.3174	39.8780
5130380	19.9830	0.0002	55009.918408	0.080312	299.1550	40.2881
5217781	564.41	0.01	55022.074166	0.109098	298.9473	40.3755
5310387	0.4416691	0.0000003	54953.664664	0.026196	299.8789	40.4824
5653126	38.4969	0.0002	54985.816152	0.067928	299.7020	40.8963
5771589	10.73914	0.00003	54962.116764	0.038736	284.5855	41.0096
6148271	1.7853	0.0001	54966.114761	0.040979	298.2297	41.4598
6197038	9.75171	0.00003	54961.776580	0.098446	289.3008	41.5265
6205460	3.72283	0.00001	54956.455222	0.098339	291.9803	41.5594
6432059	0.769740	0.000001	54964.754300	0.012775	288.0399	41.8184
6629588	2.264471	0.000003	54966.783103	0.042077	297.7556	42.0091
7289157	5.26581	0.00001	54969.976049	0.044130	293.9661	42.8373
7375612	0.1600729	0.0000001	54953.638704	0.008521	295.4670	42.9279
7668648	27.8186	0.0001	54963.315401	0.054044	286.2770	43.3391
7670617	24.7038	0.0001	54969.128128	0.044240	287.1845	43.3671
7955301	15.3244	0.0001	54968.272901	0.420237	290.1863	43.7239
8023317	16.5790	0.0001	54979.733478	0.052909	289.9703	43.8205
8122124	0.2492776	0.0000001	54964.612833	0.014220	299.0195	43.9576
8365739	2.38929	0.00000	54976.979013	0.028860	291.8875	44.3456
8758716	0.1072049	0.0000000	54953.672989	0.006195	293.8519	44.9494
8938628	6.86222	0.00002	54966.603088	0.018955	285.6626	45.2177
9214715	265.300	0.003	55149.923156	0.055997	290.3912	45.6816
9715925	6.30820	0.00003	54998.931972	0.016542	294.1644	46.4240
9834257	15.6514	0.0001	55003.014878	0.036964	293.2332	46.6002
9944907	0.613440	0.000000	54964.826351	0.021577	288.8836	46.8698
10014830	3.03053	0.00001	54967.124438	0.091901	293.1763	46.9224
10223616	29.1246	0.0001	54975.144652	0.093130	297.3907	47.2557
10268809	24.7090	0.0001	54971.999951	0.034276	289.6806	47.3178
10319590	21.3205	0.0001	54965.716743	0.085213	281.7148	47.4144
10743597	81.195	0.001	54936.094491	0.029846	296.3823	48.0453
10855535	0.1127824	0.0000000	54964.629315	0.006374	289.2119	48.2031
10919564	0.4621374	0.0000003	54861.987523	0.037827	291.5974	48.3933
11465813	670.70	0.01	55285.816598	0.302424	296.6986	49.3165
11558882	73.921	0.001	54987.661506	0.044135	291.7399	49.5708
11869052	20.5455	0.0001	54970.909481	0.022169	294.4019	50.1721
12062660	2.92930	0.00001	54998.936258	0.043481	292.0709	50.5468

Note. Those reported without BJD$_0$ errors are also heartbeat stars.

10.1. Catalog Completeness

With the primary *Kepler* mission having ended after 4 years of service, the longest orbital periods of EBs in the Catalog are ∼1000 days. Catalog completeness at those periods is challenged by our ability to detect every single eclipse event, which can be made difficult by the small eclipse amplitudes, data gaps and other intrinsic and extrinsic contributions to background and noise. Adding to this is the increasingly low probability of eclipses at the larger orbital separations that accompany longer periods, and of course the increasing probability of entirely missed eclipses for orbital periods longer than the observing window. On the other hand, completeness should be ∼100% for short period EBs ($P \sim 1$ day) because of the high geometrical probability of eclipses and because even non-eclipsing systems manifest as ellipsoidal

variables. The overall Catalog completeness is thus predominantly a function of orbital period and S/N of the eclipses. Here we only estimate completeness and defer an in-depth study that derives the underlying orbital period distribution of all binaries from the Besançon model of the Galaxy to A. Prša et al. (2016, in preparation).

To estimate Catalog completeness, we start with the observed period distribution. Figure 10 depicts the distribution of orbital periods. Two features are particularly interesting: the excess of short period binaries ($P \sim 0.3$ day) and the gradual drop-off of longer period binaries.

The short-period excess is a well-known feature of EB stars: at short periods, proximity effects become pronounced, most notably ellipsoidal variations, which enable us to detect binary stars even in the absence of eclipses. This also drives the overall probability of detection sharply upwards at shorter

Table 9
The Systems With No Repeating Events (Long) in the *Kepler* Sample

KIC	Period (%)	Event Width (days)	BJD$_0$ (−2400000)	R.A.(°) (J2000)	Decl.(°) (J2000)
2162635	0.996	1.2	55008	291.9776	37.5326
3346436	0.84	0.9	55828	292.4968	38.4627
3625986	0.75	12	55234	284.7664	38.7935
4042088	0.983	0.4	55449	286.8895	39.1074
4073089	0.67	0.7	56222	295.4901	39.1059
4585946	0.89	0.8	54969	297.3779	39.6685
4755159	0.9	0.8	55104	294.1376	39.8821
5109854	0.87	0.5	55125	294.6938	40.292
5125633	0.92	0.4	55503	298.1539	40.2474
5456365	0.95	0.7	56031	294.1284	40.6823
5480825	0.992	1.5	55194	299.5369	40.6708
6751029	0.88	0.3	55139	281.3179	42.2645
6889430	0.87	2	55194	298.3608	42.3808
7200282	0.945	0.4	55632	291.7615	42.7566
7222362	0.6	0.6	55284	297.5835	42.7721
7282080	0.965	0.2	55539	291.8008	42.8907
7288354	0.965	0.2	55235	293.7429	42.862
7533340	0.98	0.8	55819	293.4575	43.1115
7732233	0.8	0.2	55306	282.2236	43.4657
7875441	0.93	1	55534	284.9639	43.6527
7944566	0.8	0.5	55549	285.1083	43.7168
7971363	0.965	1.5	55507	295.6284	43.7571
8056313	0.88	1.5	56053	299.735	43.8779
8648356	0.98	0.75	55357	299.1302	44.7447
9466335	0.93	35	55334	292.4365	46.0956
9702891	0.82	1.1	55062	288.4751	46.4646
9730194	0.9	1	55277	298.7442	46.4508
9970525	0.9988	0.3	54972	298.7442	46.8301
10058021	0.985	0.3	55433	283.7151	47.0321
10403228	0.955	2	55777	291.2267	47.55
10613792	0.975	0.4	55773	296.8537	47.8918
11038446	0.94	0.3	55322	295.7166	48.5419

Note. These systems do not have periods.

periods. A much broader, less pronounced, longer period peak at ∼2–3 days is typically attributed to Kozai–Lidov Cycles and Tidal Friction (KCTF; Fabrycky & Tremaine 2007). The Kozai–Lidov mechanism describes interactions with a more distant third companion on an eccentric orbit, where angular momentum is exchanged between the inner binary eccentricity and the outer orbit inclination. When the components of the inner binary are sufficiently close, tidal friction dissipates energy and tightens the pair. The high occurrence rate of stellar triples (Gies et al. 2012; Rappaport et al. 2013; Conroy et al. 2014) gives further credibility to this model.
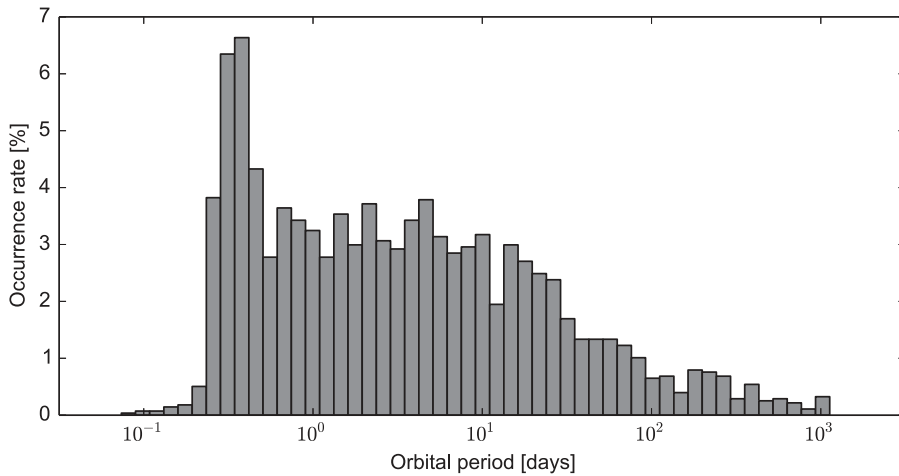
The gradual drop-off at the long period end is due to two main contributions. The dominant contribution is the geometrical probability of eclipses. Since the eccentricity distribution of *Kepler* EBs can be estimated and the pool of stellar masses and radii can be inferred from the bulk properties of all observed *Kepler* targets, computing this correction is a tractable problem. The second contribution is due to *Kepler*'s duty cycle. The satellite observed a single patch of the sky, but observations were interrupted by regular quarterly rolls and data downlink, and by unexpected events that put the telescope into safe mode. As a result, the actual duty cycle of observations was ∼92%. The dead module and targets observed only for a subset of quarters further impact completeness. We discuss each of these effects in turn and derive corresponding corrections that we use to estimate Catalog completeness. The corrections are depicted in Figure 11.
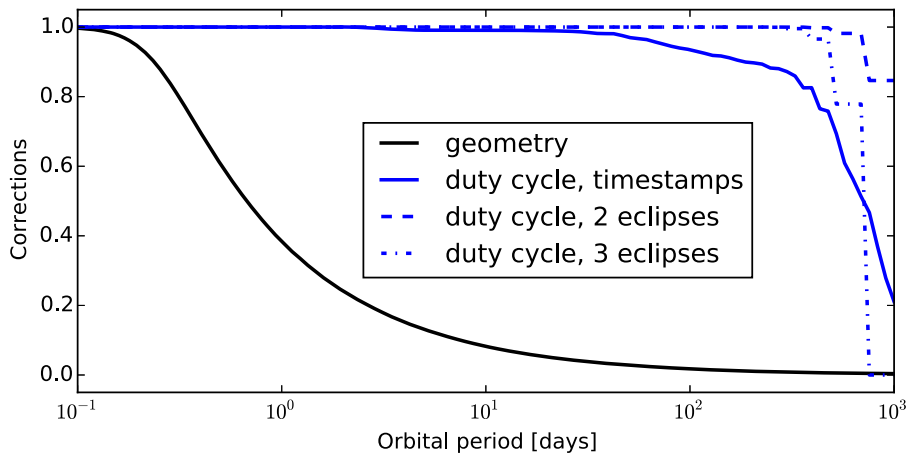
10.1.1. Geometrical Correction

The probability of eclipses is determined by a simple relation: $\cos i \leqslant (\rho_1 + \rho_2)/\delta$, where i is orbital inclination, ρ_1 and ρ_2 are fractional radii, and δ is the relative instantaneous separation. The right-hand side becomes progressively smaller with increasing orbital periods because of Kepler's 3rd law, whereas the $\cos i$ term is distributed uniformly, so the probability of eclipses drops. For eccentric orbits, the probability of eclipse at superior and inferior conjunction is $p_{\mathrm{sup,inf}} = (\rho_1 + \rho_2)(1 \pm e \sin \omega)/(1 - e^2)$. To compute it, we take all ∼200,000 stars observed by *Kepler* and create a pool based on their effective temperatures and surface gravities as reported in the Kepler Input Catalog (KIC; Brown et al. 2011). From this pool we draw pairs of stars and use the mass–radius–temperature–log(g) relationship from Torres et al. (2010) to determine the masses and radii of the drawn stars. We then place these stars in orbits with a predefined orbital period in the $-1 \leqslant \log P \leqslant 3$ range, and compute the semimajor axes. We
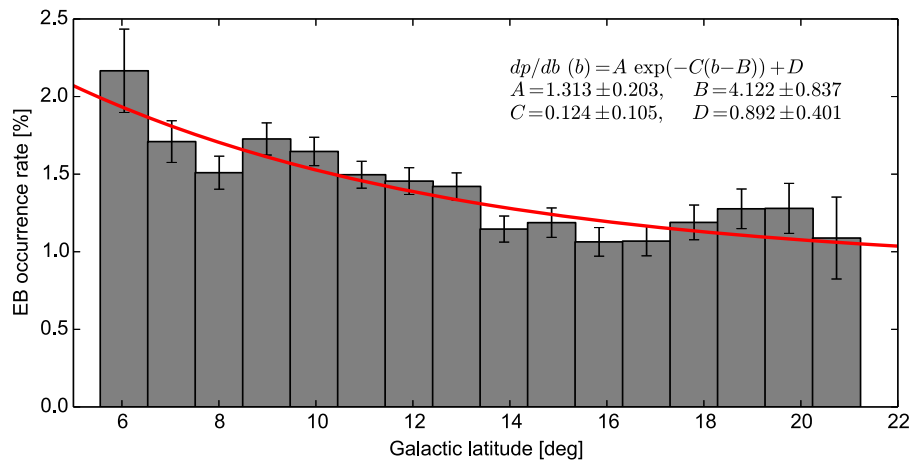
Figure 9. EB occurrence rate (dp/db) as a function of galactic latitude (b). Each latitude bin is area-corrected to give true occurrence rates. Uncertainties are estimated as $\sqrt{N_j}/N_{\mathrm{tot},j}$, where N_j is the number of detected EBs and $N_{\mathrm{tot},j}$ is the total number of targets observed by *Kepler* in the *j*th bin. The solid line represents the exponential fit to the data, with parameters annotated in the figure. The parameters A and D are occurrence rates, C is the thin-to-thick disk transition value, and B is degrees of galactic latitude. The results of this toy model indicate that the occurrence rate span of EBs ranges between 0.9% and 2.2%.

In figure:
$dp/db\,(b) = A \exp(-C(b-B)) + D$
$A = 1.313 \pm 0.203,\quad B = 4.122 \pm 0.837$
$C = 0.124 \pm 0.105,\quad D = 0.892 \pm 0.401$

Figure 10. Distribution of orbital periods of all Cataloged EBs.

Figure 11. Corrections to EB detection rates as a function of orbital period. Geometrical correction is dominant across all orbital periods, while the duty cycle correction becomes important at the long period end. The solid curve for the duty cycle correction is computed by requiring at least two eclipse events to be observed, while the dashed curve shows the duty cycle correction for at least three observed eclipse events. The combined correction is the product of individual corrections.

also account for ellipsoidal variability on the short period end and non-zero eccentricity on the long period end. The geometrical correction is depicted in Figure 11 in black.

10.1.2. Duty Cycle Correction

While *Kepler* observed approximately 200,000 stars for most of the mission, which targets were observed in which quarters varies at the 10% level for various reasons, such as compensating for missing modules and variations in target lists over time. To account for these variations and the specific duty cycle, we performed a detailed analysis that leads to a global window function. As an approximation to the search of our algorithm, we use the Transiting Planet Search (TPS) deweighting vector (Burke et al. 2015) to determine which cadences are actually observed by *Kepler*. This correctly accounts for the exact gaps in the data.

For every target, we use the online stellar table to identify the quarters for which observations were taken. We then scan over periods ranging from 0.5 to 1500 days, with a trial period corresponding to integer number of *Kepler* cadences (30 minutes). For each period, we also scan over every possible phase (again, in integer cadences) and determine the fraction of phases where *Kepler* acquired data on this target. This creates an individual window function for each target that corresponds

to the probability that an EB with a random phase would have had at least two observations as a function of period, which is the minimum requirement to determine the ephemeris of the system. We then sum these individual window functions to determine, for every period, how many *Kepler* targets would have two observations. The correction as a function of period is depicted in Figure 11 in solid blue.

It is instructive to compare this window function to the theoretical window function if we assume a uniform observing completeness of 92%. Assuming that an EB was observed for all quarters, the probability of observing any single eclipse is 92%, and the probability for an eclipse to fall into a data gap is 8%. The effect is smaller for intermediate period binaries and diminishes for shorter period systems. A binary with an orbital period of ~1000 days will have 2 primary eclipse events in the data, a binary with an orbital period of ~250 days will have 5 eclipse events, and a ~100-day binary will have 14 events. Thus, the probability of a significant fraction of 14 events falling into data gaps is negligibly small, while the effect on 5 events, and especially 2 events, can be dire.

The probability that two or more eclipses were observed is calculated by a binomial expression that depends on the duty cycle and on the number of eclipses, which in turn depends on the orbital period. To compute that probability, it is simpler to
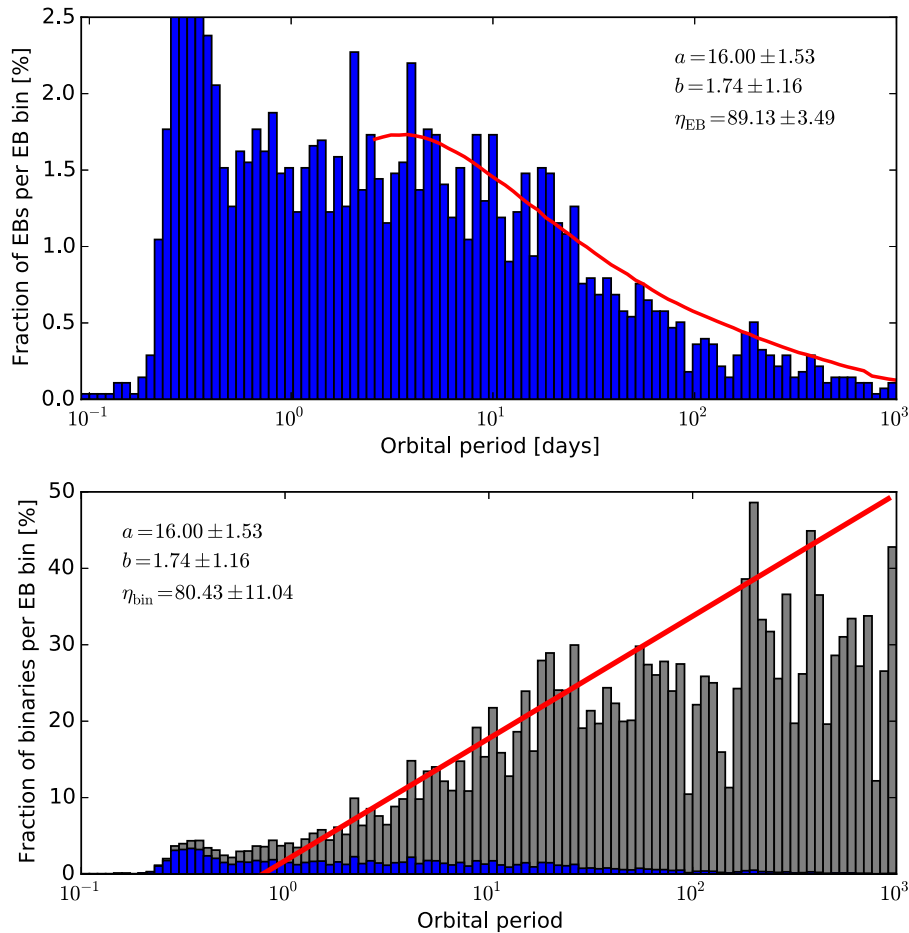
Figure 12. Completeness estimates for the EB Catalog (top), and projected completeness estimates for the binary star population (bottom). The observed distribution of orbital periods is depicted in blue, and the theoretical distribution of orbital periods, derived from a linear model of the underlying binary log-period distribution, is depicted in red. The distribution depicted in gray is the predicted occurrence rate of *all* binary stars based on *Kepler* data, compared to the best-fit linear model.

compute the probability that no eclipses are detected or that only one eclipse is detected, and take the complement: $p_{detection} = 1 - p_0 - p_1 = 1 - (0.08)^N - N(0.92)^1(0.08)^{N-1}$, where N is the number of eclipses. *Kepler* accumulated 1460 days of data, so N can be written as $1 + \text{int}(1460/P)$, where P is the orbital period. We expect a cascading correction with a discrete jump at every period that changes the integer division value. This correction is depicted in Figure 11 in dashed blue.

If we were to require a detection of three eclipses, we would need to subtract another binomial term from the probability equation, $p_2 = 0.5N(N-1)(0.92)^{N-2}(0.08)^2$, which further reduces the detection rate. This correction is depicted in Figure 11 in dash–dotted blue.

10.1.3. Combined Correction

The combined correction, ϵ_C, is a product of individual corrections: $\epsilon_C = \epsilon_G \epsilon_{DC}$. If we knew what the underlying distribution of all (not just eclipsing) binary stars is, then multiplying that distribution with ϵ_C would provide us with a theoretical prediction for the observed number of EBs by *Kepler*. The *actual* number of EBs observed by *Kepler*, divided by the *predicted* number of EBs observed by *Kepler*, is then the measure of Catalog completeness.

We do not know the underlying distribution of binary stars, but we can approximate it for the purpose of this estimate. Several works, most notably Duquennoy & Mayor (1991) and

Kroupa & Burkert (2001), report a log-Gaussian distribution with the peak well in excess of 10,000 days. We are thus sampling a far tail of the left wing, and we can assume that the distribution in the $1.3 \leqslant \log P \leqslant 3$ range is locally[38] linear, $dB/d(\log P) = a \log P + b$. By making that assumption, we can then: (1) set a and b to some reasonable initial values; (2) derive the EB distribution function $dEB/d(\log P) = \epsilon_C \times dB/d(\log P)$; (3) compare this theoretical prediction with the observed distribution, and (4) iterate a and b to obtain the best-fit values on the linear $\log P$ range. Figure 12 depicts this comparison: the top plot shows the comparison between the observed EB period distribution (blue bars) and theoretical prediction in the $1.3 \leqslant \log P \leqslant 3$ range (solid red line), and the bottom plot shows the comparison between the backwards-projected $dB/d(\log P) = dEB/d(\log P)/\epsilon_C$ (gray bars) and the assumed underlying linear distribution (red line). To get the completeness estimates, we divide the integral of the observed trend with the integral of the predicted trend. We do not take the short period excess into account because of its extrinsic causes. The annotations in the plots give the best-fit parameters and the derived completeness rates. The completeness of

---

[38] Tidal interaction and the Kozai–Lidov mechanism prohibit this toy model from working below $\log P \sim 1.3$, which is why we do not attempt to model the short period end; since it is reasonable to assume that the Catalog is essentially complete on that end, this deviation from the model bears no significant impact on our completeness result.

cataloged EBs is $\eta_{EB} = 89.1\% \pm 3.5\%$, and completeness of all binaries is $\eta_{bin} = 80\% \pm 11\%$.

11. SUMMARY

This revision of the Catalog contains new additions consisting of rejected KOIs, previously misidentified false positives, proprietary systems, updated long period systems, EBs identified from other systems, heartbeat stars, and Planet Hunters' systems. Detrended and phased long-cadence data are hosted and available for the public, as well as an updated period for each system adjusted to account for ETVs. We also provide a deconvolved polyfit which serves as a better approximation of the actual light curve and a classification parameter representing the morphology of the phased light curve. A Catalog analysis including a completeness study is provided.

An online version of the Catalog is maintained at http://keplerEBs.villanova.edu. This Catalog lists the KIC, ephemeris, morphology, principle parameters, polyfit data, ETV data, raw data, and an array of figures displaying the raw time domain, detrended data, and phased light curves of each system along with period frequency, ETV, and diagnostic analysis plots. The online Catalog also provides a visualization tool to further exploit this data set. It is our hope that the Catalog will serve the EB community as a bridge between the raw *Kepler* data and in-depth scientific modeling.

Facility: Kepler.

APPENDIX
THE ONLINE CATALOG

The online Catalog provides a searchable database of all the EBs found in the entire *Kepler* data set along with downloadable content and visualization tools. The online version of the Catalog is currently maintained at http://keplerEBs.villanova.edu. The homepage presents the user with a view of the entire EB catalog. Along the top tool-bar is the tab, "Search" which provides a page where the Catalog can be filtered, sorted, and exported with a variety of options: ID numbers, eclipse properties, morphology parameter, location elements, ETV properties, effective temperatures, and flags with the ability to export the results to something other than the default HTML table, if desirable. For a complete list of search options, units and explanations, and exporting formats please see the online Help section.

For individual EB entries, the online Catalog provides a summary of the EB's physical properties, analytic plots, and provides the time-series data for download in various formats. In addition to the raw data, the polyfit data used to detrend the time-series data and the ETV data, along with the suite of diagnostic figures are available for download. The figures provided for each EB entry are: raw data, detrended data, polyfit, ETV, and TPF plots. If available, the individual entry page shows additional spectral observations available for download and any publications concerning that EB entry.

The Catalog currently maintained at http://keplerEBs.villanova.edu will continue to evolve as additional data is ingested and new techniques enhance our research capabilities. A static version of the online Catalog associated with this paper is maintained at MAST https://archive.stsci.edu/kepler/eclipsing_binaries.html.

REFERENCES

Anderson, A. 1991, A&ARv, 3, 91
Batalha, N. M., Borucki, W. J., Koch, D. G., et al. 2010, ApJL, 713, L109
Bonanos, A. Z., Stanek, K. Z., Kudritzki, R. P., et al. 2006, ApJ, 652, 313
Bonanos, A. Z., Stanek, K. Z., Sasselov, D. D., et al. 2003, AJ, 126, 175
Borucki, W. J., Koch, D. G., Basri, G., et al. 2011, ApJ, 736, 19
Brown, T. M., Latham, D. W., Everett, M. E., & Esquerdo, G. A. 2011, AJ, 142, 112
Burkart, J., Quataert, E., Arras, P., & Weinberg, N. N. 2012, MNRAS, 421, 983
Burke, C. J., Christiansen, J. L., Mullally, F., et al. 2015, ApJ, 809, 8
Caldwell, D. A., Kolodziejczak, J. J., Van Cleve, J. E., et al. 2010, ApJL, 713, L92
Carter, J. A., Fabrycky, D. C., Ragozzine, D., et al. 2011, Sci, 331, 562
Claret, A., & Gimenez, A. 1993, A&A, 277, 487
Claret, A., & Giménez, A. 2010, A&A, 519, A57
Conroy, K. E., Prša, A., Stassun, K. G., et al. 2014, AJ, 147, 45
Coughlin, J. L., Thompson, S. E., Bryson, S. T., et al. 2014, AJ, 147, 163
Croll, B., Rappaport, S., & Levine, A. M. 2015, MNRAS, 449, 1408
Deeg, H. J., Doyle, L. R., Kozhevnikov, V. P., et al. 1998, A&A, 338, 479
Doyle, L. R., Carter, J. A., Fabrycky, D. C., et al. 2011, Sci, 333, 1602
Doyle, L. R., Deeg, H. J., Kozhevnikov, V. P., et al. 2000, ApJ, 535, 338
Duquennoy, A., & Mayor, M. 1991, A&A, 248, 485
Fabrycky, D., & Tremaine, S. 2007, ApJ, 669, 1298
Feiden, G. A. 2015, in ASP Conf. Ser. 496, ed. S. M. Rucinski, G. Torres, & M. Zejda (San Francisco, CA: ASP), 137
Fischer, D. A., Schwamb, M. E., Schawinski, K., et al. 2012, MNRAS, 419, 2900
Fuller, J., & Lai, D. 2012, MNRAS, 420, 3126
Gies, D. R., Williams, S. J., Matson, R. A., et al. 2012, AJ, 143, 137
Gimenez, A. 1985, ApJ, 297, 405
Guinan, E. F., Fitzpatrick, E. L., DeWarf, L. E., et al. 1998, ApJL, 509, L21
Guinan, E. F., Ribas, I., Fitzpatrick, E. L., et al. 2000, ApJ, 544, 409
Hambleton, K., Degroote, P., Conroy, K., et al. 2013, in EAS Publications Ser. 64, ed. K. Pavlovski, A. Tkachenko, & G. Torres, 285
Hartman, J. 2012, Astrophysics Source Code Library, ascl:1208.016
Hilditch, R. W., Howarth, I. D., & Harries, T. J. 2005, MNRAS, 357, 304
Huber, D., Silva Aguirre, V., Matthews, J. M., et al. 2014, ApJS, 211, 2
Jenkins, J. M. 2002, ApJ, 575, 493
Jenkins, J. M., Chandrasekaran, H., McCauliff, S. D., et al. 2010, Proc. SPIE, 7740, 0
Koch, D. G., Borucki, W. J., Basri, G., et al. 2010, ApJL, 713, L79

Kostov, V. B., McCullough, P. R., Carter, J. A., et al. 2014, ApJ, 787, 93
Kovács, G., Zucker, S., & Mazeh, T. 2002, A&A, 391, 369
Kroupa, P., & Burkert, A. 2001, ApJ, 555, 945
Kumar, P., Ao, C. O., & Quataert, E. J. 1995, ApJ, 449, 294
Lintott, C. J., Schawinski, K., Slosar, A., et al. 2008, MNRAS, 389, 1179
Lomb, N. R. 1976, Ap&SS, 39, 447
Maaten, L., & Hinton 2008, Journal of Machine Learning Research, 9, 2579
Maceroni, C., Montalbán, J., Michel, E., et al. 2009, A&A, 508, 1375
Matijevič, G., Prša, A., Orosz, J. A., et al. 2012, AJ, 143, 123
Meibom, S., & Mathieu, R. D. 2005, ApJ, 620, 970
Mighell, K. J., & Plavchan, P. 2013, AJ, 145, 148
Mullally, F., Coughlin, J. L., Thompson, S. E., et al. 2015, ApJS, 217, 31
North, P., Gauderon, R., Barblan, F., & Royer, F. 2010, A&A, 520, A74
Orosz, J. A. 2012, in American Astronomical Society Meeting Abstracts 220, 406.02
Orosz, J. A. 2015, arXiv:1503.07295
Orosz, J. A., & Hauschildt, P. H. 2000, A&A, 364, 265
Orosz, J. A., Welsh, W. F., Carter, J. A., et al. 2012a, Sci, 337, 1511
Orosz, J. A., Welsh, W. F., Carter, J. A., et al. 2012b, ApJ, 758, 87
Parvizi, M., Paegert, M., & Stassun, K. G. 2014, AJ, 148, 125
Pols, O. R., Tout, C. A., Schroder, K.-P., Eggleton, P. P., & Manners, J. 1997, MNRAS, 289, 869
Prša, A., Batalha, N., Slawson, R. W., et al. 2011, AJ, 141, 83
Prša, A., Guinan, E. F., Devinney, E. J., et al. 2008, ApJ, 687, 542
Prša, A., Robin, A., & Barclay, T. 2015, IJAsB, 14, 165
Prša, A., & Zwitter, T. 2005, ApJ, 628, 426

Rappaport, S., Deck, K., Levine, A., et al. 2013, ApJ, 768, 33
Ribas, I., Fitzpatrick, E. L., Maloney, F. P., Guinan, E. F., & Udalski, A. 2002, ApJ, 574, 771
Rowe, J. F., Borucki, W. J., Koch, D., et al. 2010, ApJL, 713, L150
Roweis, S. T., & Saul, L. K. 2000, Sci, 290, 2323
Scargle, J. D. 1982, ApJ, 263, 835
Schroder, K.-P., Pols, O. R., & Eggleton, P. P. 1997, MNRAS, 285, 696
Schwamb, M. E., Orosz, J. A., Carter, J. A., et al. 2013, ApJ, 768, 127
Schwarzenberg-Czerny, A. 1989, MNRAS, 241, 153
Slawson, R. W., Prša, A., Welsh, W. F., et al. 2011, AJ, 142, 160
Stassun, K., Paegert, M., De Lee, N. M., & Cargile, P. 2013, in American Astronomical Society Meeting Abstracts 221, 116.01
Thompson, S. E., Everett, M., Mullally, F., et al. 2012, ApJ, 753, 86
Torres, G., Andersen, J., & Giménez, A. 2010, A&ARv, 18, 67
Torres, G., & Ribas, I. 2002, ApJ, 567, 1140
Welsh, W. F., Orosz, J. A., Aerts, C., et al. 2011, ApJS, 197, 4
Welsh, W. F., Orosz, J. A., Carter, J. A., et al. 2012, Natur, 481, 475
Welsh, W. F., Orosz, J. A., Carter, J. A., & Fabrycky, D. C. 2014, in IAU Symp. 293, ed. N. Haghighipour, 125
Welsh, W. F., Orosz, J. A., Short, D. R., et al. 2015, ApJ, 809, 26
Willems, B., & Aerts, C. 2002, A&A, 384, 441
Wilson, R. E. 1979, ApJ, 234, 1054
Wyithe, J. S. B., & Wilson, R. E. 2001, ApJ, 559, 260
Wyithe, J. S. B., & Wilson, R. E. 2002, ApJ, 571, 293
Zahn, J.-P. 1975, A&A, 41, 329
Zahn, J.-P., & Bouchet, L. 1989, A&A, 223, 112